Geophysical Journal International

Geophys. J. Int. (2014) **196,** 1375–1396
Advance Access publication 2014 January 16

doi: 10.1093/gji/ggt486

Chemical and magnetic properties of rapidly cooled metastable ferri-ilmenite solid solutions – IV: the fine structure of self-reversed thermoremanent magnetization

Peter Robinson,[1] S. A. McEnroe,[2,3] K. Fabian,[1] R. J. Harrison,[4] C. I. Thomas[3] and H. Mukai[5]

[1] *Geological Survey of Norway, N-*7491 *Trondheim, Norway*
[2] *Norwegian University of Science and Technology, N-*7491 *Trondheim, Norway. E-mail: suzanne.mcenroe@ntnu.no*
[3] *Department of Chemistry, University of Oslo, Oslo, Norway*
[4] *Department of Earth Sciences, University of Cambridge, Cambridge CB*2 3*EQ, UK*
[5] *Institut für Mineralogie, Münster* 48149*, Germany*

Accepted 2013 November 28. Received 2013 November 20; in original form 2013 July 2

SUMMARY

Magnetic experiments, a Monte Carlo simulation and transmission electron microscopy observations combine to confirm variable chemical phase separation during quench and annealing of metastable ferri-ilmenite compositions, caused by inhomogeneous Fe-Ti ordering and anti-ordering. Separation begins near interfaces between growing ordered and anti-ordered domains, the latter becoming progressively enriched in ilmenite component, moving the Ti-impoverished hematite component into Fe-enriched diffusion waves near the interfaces. Even when disordered regions are eliminated, Fe-enriched waves persist and enlarge on anti-phase boundaries between growing and shrinking ordered and anti-ordered domains. Magnetic results and conceptual models show that magnetic ordering with falling T initiates in the Fe-enriched wave crests. Although representing only a tiny fraction of material, identified at highest Ts on a field-cooling curve, they control the 'pre-destiny' of progressive magnetization at lower T. They can provide a positive magnetic moment in a minority of ordered ferrimagnetic material, which, by exchange coupling, then creates a self-reversed negative moment in the remaining majority. Four Ts or T ranges are recognized on typical field-cooling curves: T_{PD} is the T range of 'pre-destination'; T_C is the predominant Curie T where major positive magnetization increases sharply; T_{MAX} is where magnetization reaches a positive maximum, beyond which it is outweighed by self-reversed magnetization and T_{ZM} is the T where total magnetization passes zero. Disposition of these Ts on cooling curves indicate the fine structure of self-reversed thermoremanent magnetization. These results confirm much earlier suspicions that the 'x-phase' responsible for self-reversed magnetization resides in Fe-enriched phase boundaries.

Key words: Magnetic mineralogy and petrology; Rock and mineral magnetism; Microstructures; Phase transitions.

1 INTRODUCTION

The microstructures produced by Fe-Ti ordering in quenched and annealed ferri-ilmenite solid solutions were portrayed in the landmark transmission electron microscopy (TEM) studies by Nord & Lawson (1989, 1992), who implied, but did not demonstrate, chemical phase separation during this process. More recently chemical evolution of quenched and annealed ferri-ilmenite solid solutions was covered in some detail by Robinson *et al*. (2012a), in general agreement with the earlier results of Harrison (2006). Emphasis was placed on the details of 'contact layers' expected to be found at interfaces between ordered and anti-ordered phases, even where the two are of the same composition and the same order parameter Q. Arguments were also made that, after metastable chemical phase separation, the coarsening process will cause small and shrinking ordered and anti-ordered domains to become more Fe-enriched relative to larger and growing ordered and anti-ordered domains. Further, it was postulated that the vicinity of the antiphase boundaries between the ordered and anti-ordered domains will become even more Fe-rich than the Fe-rich domain they are adjacent to, thus creating Fe-enriched 'waves'.

Recent high-temperature (T) magnetic experiments shed new light on the acquisition of self-reversed thermoremanent magnetization in such samples. Extensive background for this subject is covered by Fabian *et al*. (2011), including discussion of many earlier studies (Nagata *et al*. 1952; Uyeda 1958; Ishikawa & Syono 1963;

Hoffman 1975a,b, 1992; Prévot *et al*. 2001; Ozima *et al*. 2003; Lagroix *et al*. 2004). Basic features of the magnetic interactions, as presently understood, are described by Robinson *et al*. (2012b). Here we describe four types of magnetic experiments on two synthetic samples, a Monte Carlo simulation, and TEM observations. Conceptual models are then provided that link chemical evolution to the details of self-reversed thermoremanent magnetization.

2 MAGNETIC EXPERIMENTS, SIMULATIONS, TEM OBSERVATIONS

Magnetic measurements were made using a Vibrating Sample Magnetometer (VSM, Princeton Measurements Corp., Princeton, NJ, USA). These included switching-*T* experiments (Section 2.1), cooling curves (Section 2.2), hysteresis loops at *T* (Section 2.3) and high- and low-*T* measurements of susceptibility and remanence (Section 2.4). Switching-*T* experiments and cooling curves were made by heating a sample to a maximum *T* of 350 °C, and then cooling to room temperature (RT) in a + or – field of 0.5 or 5 mT. Low-*T* measurements were made at the IRM (University of Minnesota, Minneapolis, MN, USA) from RT down to 10 K with a liquid helium cryostat inserted in the VSM. *T*-hysteresis loops were measured in a sequence after heating the sample first to 350 °C, and then cooling to the indicated temperature, followed by a wait time of 3 min, inside the He flow of the VSM furnace. A field of 1 Tesla (T) was applied for the hysteresis measurements.

2.1 Switching-*T* experiments

In these experiments, first introduced by Fabian *et al*. (their fig. 10, Fig. 1 here), the sample was cooled in a field of –0.5 mT, from 350 °C, a *T* below which chemical change will not occur. The 'switching *T*', is the *T* where the field was switched from –0.5 to +0.5 mT, after which the sample was cooled to RT, where the remanence was measured. It was observed that if the switch occurred above a certain *T* range, then the resulting remanence at RT was negative. However, below that *T* range, the switch to a positive field had no effect, and the resulting remanence at RT was positive. In this way a *T* range was identified where the primary requirement for magnetic self-reversal was established, yielding negative remanence when the magnetization was positive while passing this, and yielding positive remanence when the magnetization was negative while passing the same *T* range.

For a sample of bulk composition Ilm 60 (Fig. 1a), quenched at 900 °C, above the 830 °C cation ordering *T*, and annealed for 5 min at 600 °C, below the cation ordering *T*, the corresponding *T* range is 285–250 °C equivalent to the Curie *T*s of the compositions Ilm 49–53. For a sample of bulk composition Ilm 65 (Fig. 1b) quenched at 980 °C, above the 915 °C cation ordering *T* and annealed for 1 min at 600 °C, below the cation ordering *T*, the corresponding *T* range is 255–150 °C equivalent to the Curie *T*s of the compositions Ilm 52.5–63. For a sample of bulk composition Ilm 61 annealed for a few seconds, as in fig. 10 of Fabian *et al*. (2011), this *T* range, 220–175 °C, equivalent to the Curie *T*s of the compositions Ilm 56–61, was referred to as the 'self-reversal *T*', which we redefine here.

The *T* ranges over which the self-reversal is 'pre-destined', 285–250 °C for B-06, and 255–150 °C for B-20, correspond in Curie *T*s to the composition ranges Ilm 49–53, and Ilm 52.5–63, which are distinctly more Fe-rich than the Ilm 60 and Ilm 65 bulk compositions, respectively. This provides the argument that Fe-enrichment along phase-domain boundaries, commonly in antiphase relationship, 'pre-destine' the future of self-reversal at *T*s distinctly above the Curie *T*s of the bulk samples. The larger *T* range for B-20 compared to B-06 indicates a larger variation in the degree of Fe-enrichment along the domain boundaries. The 'pre-destination' *T* is equivalent to the blocking *T* of the '*x*-phase' in the conventional terminology used in self-reversal models.

2.2 Cooling curves

In cooling-curve experiments (Figs 2a and b), the sample was heated to 350 °C and then cooled slowly in a weak field of 0.5 mT, with the magnetization measured at 5 °C intervals, allowing 10 or 20 s for thermal equilibration between measurements. At *T*s close to the supposed 'self-reversal *T*', the measured remanence was very close to zero, implying antiferromagnetic behaviour. At slightly lower *T* on the cooling curves of Figs 2(a) and (b), there was a sharp increase in magnetization, proceeding to substantial values with continued cooling, so that a Curie *T* could be estimated by conventional means, here indicated 'T_C'. The sharp rise of positive magnetization tailed off to a broad peak ('T_{MAX}') and then began to fall. First observations suggested the beginning of negative magnetization was occurring, and this also was temporarily identified as the 'self-reversal *T*' (Fabian *et al*. 2011). This is commonly more than 100 °C lower than the 'pre-destination *T*' described here for the 'switching-*T*' experiments. With further cooling, the positive net magnetization progressively decreased, reaching 0, and continued to decrease to a very negative value by RT, resulting in a net self-reversed magnetization.

To a first approximation we can now identify four significant *T*s in these materials with progressive cooling: (1) The *T* that determines the self-reversed remanence acquired on cooling to RT, here called the 'magnetic pre-destination *T*' or 'T_{PD}'. This *T* or, more commonly, *T* range, controls the final magnetic destiny, even though the bulk magnetization at this stage is very weak. We show that this *T* range is intimately associated with phase-domain boundaries and/or antiphase domain boundaries (APBs) in this material. The 'PD' in the name can equally be related to 'phase domain'. (2) A *T* that corresponds to a T_C at the onset of positive magnetization of a significant fraction of ferrimagnetic material. (3) A *T* at the positive maximum (T_{MAX}) for the thermal curve, a point where negative magnetization begins to overwhelm the previously acquired positive magnetization. This is not a 'self-reversal *T*' for several reasons. Some antiphase domains (APDs) already acquired negative magnetization at a higher *T*, but not enough to overwhelm the positive magnetization acquired earlier. This is not where the net magnetization becomes negative, only where it begins the trip towards final domination, that is, T_{MAX}. (4) At a much lower *T* the magnetization passes a value of zero, and enters the region of 'true self-reversal', with the magnetization continuing towards even more negative values with further cooling to RT. We suggest that the *T*, where the curve crosses zero, so that bulk reversal is acquired, be called the 'zero magnetization *T*', or 'T_{ZM}'. These *T* s are shown in Figs 2(a) and (b).

For B-06, the entire T_{PD} range, derived in Fig. 1(a), lies ∼10 °C above T_C, at a *T* where net magnetization is very weak. For B-20, the entire T_{PD} range, derived in Fig. 1(b), begins ∼60 °C above T_C, at a *T* where net magnetization is very weak, but extends downward to just above T_{MAX}. This is interpreted to reflect the variety of compositions along Fe-enriched domain boundaries, so that self-reversed magnetization began early in some places along these boundaries, and at much lower temperature in others.

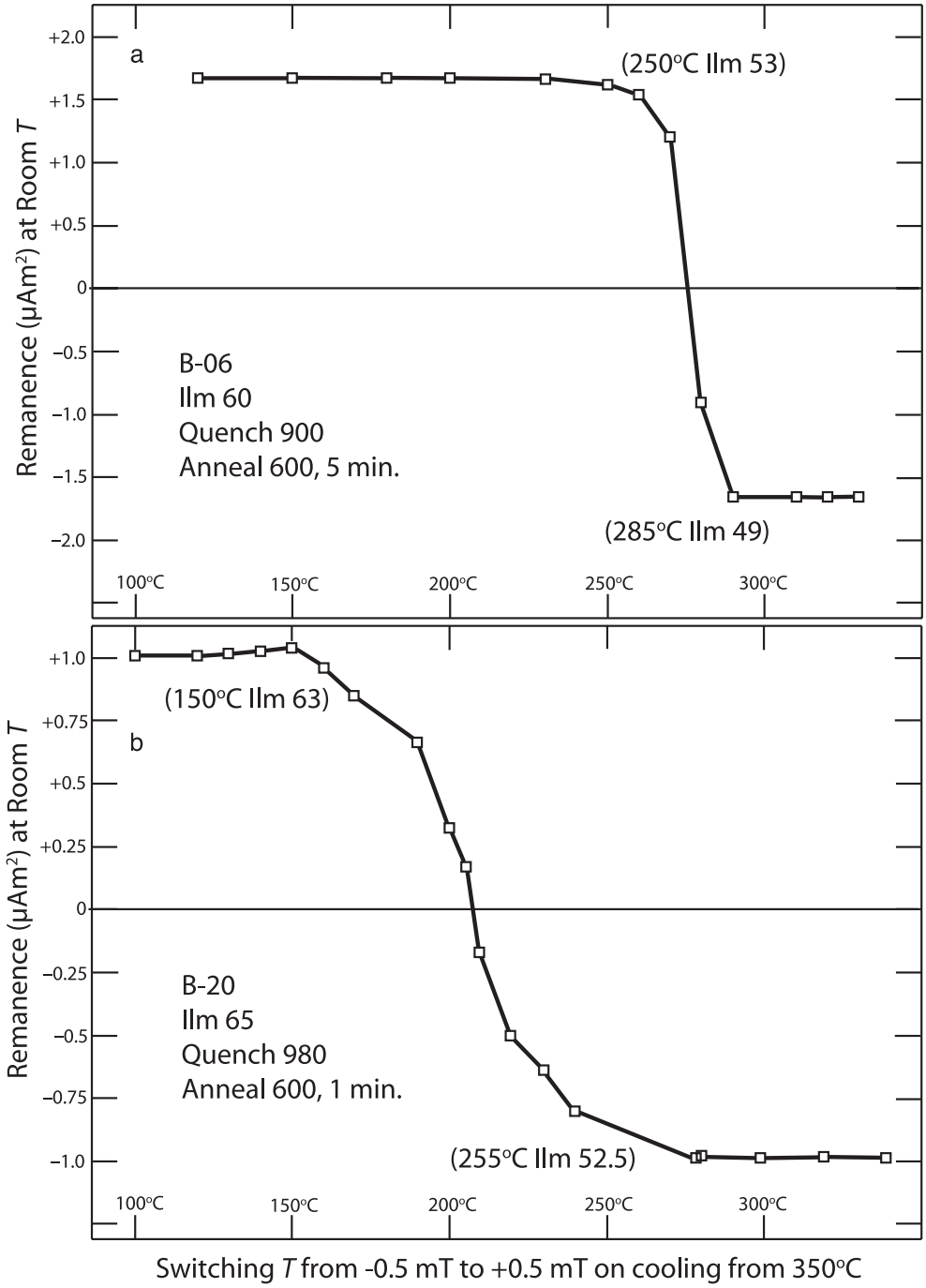

Figure 1. Results of switching-*T* experiments for samples B-06 and 20. Each point on the graphs represents remanence in μT measured at RT at the end of a single cooling experiment beginning in a field of –0.5 mT at 350 °C followed by switching to a field of +0.5 mT at the indicated *T*. For sample B-06 resulting remanence was ∼ –1.7 μT where switching was 285 °C and above (self-reversal in a positive field), and ∼ +1.7 μT where switching was 250 °C and below (self-reversal in a negative field). For sample B-20 resulting remanence was ∼ –1 μT where switching was 255 °C and above, and ∼1 μT where switching was 150 °C and below. Where the switch was done at intermediate *T*s, some compositions in the sample magnetized in a negative field and others in a positive field yielding an intermediate remanence at RT (see text for implications).

Fig. 2(c) shows the results of a different cooling experiment made on sample B-06. Here, at each temperature, beginning 350 °C (623 K), and extending down to 10 K in steps of 2 K, a magnetization curve between $H = 0$ and 5 mT in steps of 0.2 mT was measured. From quadratic least-square fits of the data to the equation $f(H) = m + \chi H + bH^2$, it is at each temperature possible to determine both susceptibility (χ), and remanence (m). The remanence curve imitates most of the general features of Fig. 2(a), that shows magnetic moment within the inducing cooling field, combining susceptibility and remanence. The comparison confirms that indeed remanence dominates the induced signal. The curve of susceptibility in Fig. 2(c) shows a steep upward rise at 240 °C, corresponding to the point marked T_C in Fig. 2(a), and a local peak at about 222 °C. The curves of Figs 2(a) and (b), and the remanence curve in Fig. 2(c) all show a strong downward increase in negative magnetization or remanence, a phenomenon not yet fully

understood. In Fig. 2(c) this continues down to about 30 K, where slope changes in both χ and m suggest phenomena we have reported earlier (Robinson *et al*. 2010) that are possibly related to low-T magnetization of ilmenite-like clusters in the solid solution.

Similar cooling curves have been published earlier. Prévot *et al*. (2001) show curves for natural samples from Pinatubo Volcano (their fig. 3), one for the rock containing significant magnetite, and one for a separated hemo-ilmenite single crystal, where they estimate a bulk composition $X = 0.53$. Using our terminology, T_C is ∼240 °C, $T_{MAX} \sim 200$ °C and $T_{ZM} \sim 140$ °C. $T_C = 240$ °C implies that a significant fraction of the sample has composition $X = 0.54$ or greater. Lagroix *et al*. (2004) show two curves for $X = 0.70$ samples (their fig. 8) originally studied in TEM by Nord & Lawson (1989), Q1300 quenched from 1300 °C, and Q1050 quenched from 1050 °C. Q1300 provides excellent evidence for self-reversal though the drawing scale makes temperature picks difficult. Q1050, containing a much better developed quench microstructure, shows $T_C \sim 107$ °C, $T_{MAX} \sim 92$ °C and $T_{ZM} \sim 62$ °C. $T_C = 107$ °C implies that a significant fraction of the sample has composition $X = 0.67$ or greater.

2.3 Hysteresis loops at T

Hysteresis loops (Fig. 3) were measured on sample B-06 during a sequence involving initial heating from RT (30 °C) to 350 °C and then cooling in a field of +0.5 mT to 280 °C where the first hysteresis loop was run. The sample was then cooled successively, in the absence of an applied field, to Ts of 240, 220, 200, 180, 140, 120, 100, 80, 60, 40 and 30 °C, where hysteresis loops were measured. Seven of these are shown in Fig. 4 and their Ts are marked on the cooling curve of Fig. 2(a). A second sequence of loops (not shown) was measured with cooling in a field of +0.5 mT. Surprisingly, the general loop shapes are not dramatically different than those in Fig. 3, though with slightly shifted positions due to remanence. This suggests that initial remanence, induced in the T_{PD} range, controls most of the subsequently acquired remanence. The values labelled M_s in each panel are the intercepts on the vertical axis in a field of +1 T and are simply for comparative purposes. This material is very far from saturated in a 1 T field. However, the value M_s provides a guide to the increasing amount of magnetization induced by a 1 T field with progressively lower T_S. This is in contrast to M_r (remanence), which increases to a T of 170 °C, decreases to zero between 60 and 80 °C, then increases again (negative values) at still lower T as shown in Fig. 2(c). For each loop except 280 °C, inflection points (black dots) were calculated from the average of the upper and lower branches. The loops mainly reflect the APD microstructure and interface interactions at each T.

The loop at 280 °C is essentially straight. Any ferromagnetic moment would be less than 15 nAm^2 and not detectable at this enlarged vertical scale. It lies near the upper limit of the T_{PD} range at 285 °C (Fig. 1a) suggesting that a very small fraction of the sample has a composition adequate to acquire a very weak ferrimagnetic moment at this T, whereas the bulk of the sample is either paramagnetic or close to being antiferromagnetic.

The loops at 220, 200 and 180 °C are on the rising part of the cooling curve of Fig. 2(a). This shows that the magnetization of the ferrimagnetic component at these Ts aligns positively with the previously applied field, thereby adding to the weak component as shown by the T_{PD} curve at higher T. Henceforward, this is referred to as a positive ferrimagnetic component. In this interval H_c, M_r and M_s all increase together. At 220 °C the inflection points are far apart, but they converge quickly with falling T to 200 °C and remain similar at 180 °C. This is interpreted as due to rapid increase in importance of the positive ferrimagnetic component. Outside the inflection points in all three, the slight tendency to slope flattening likely continues to higher fields.

The loops measured at 140, 100 and 60 °C are below T_{MAX}, where self-reversed magnetization on the cooling curve of Fig. 2(a) starts to outweigh the antiferromagnetically coupled positive magnetization. The central opening, already widening at 180 °C becomes progressively still wider in the steps towards 60 °C, indicating increasing antiferromagnetic coupling between the initial positive ferrimagnetic component and the self-reversed ferrimagnetic component as shown on the cooling curve. Following the 180 °C loop, the subtle calculated inflection points move progressively outward with falling temperature at 140 °C to 30 °C. Inside the inflection points these four loops show unusual steepening in slope, not a tendency towards saturation, undoubtedly related to APDs with opposed magnetizations. In the interval 140 °C to 60 °C, M_r decreases progressively, consistent with progressive subtraction of negative from positive magnetization to T_{ZM}, while M_s continues to increase consistent with falling T. In the last loop at 30 °C, below T_{ZM}, M_r starts to increase again because negative magnetization has come to dominate.

The loops at 60 and 30 °C, both show a positive exchange bias, as well as a larger opening in the negative than in the positive quadrant. While it is not easy to estimate the local field strength when the remanence was acquired in this sample, the positive hysteresis shift at both temperatures is the same as predicted from cooling in a positive field in magnetic models we constructed (Robinson *et al*. 2012b) and the same as measured by Meikeljohn & Carter (1959).

An intriguing feature of the thermal sequence in Fig. 3 is that it mimics sequences we have recorded at RT involving changes in composition Ilm 60–65–70, in quench time, and in annealing time. Here the lowest-T curves are like RT curves for poorly evolved Ilm 60 samples, where the inflection points are widely separated, and highest temperature curves mimic RT curves for somewhat more evolved Ilm 65, 70 samples, where inflection points are much closer to the origin. In both data sets the inflection point positions are significant. Concave-down curvature in the positive field quadrant implies movement towards saturation in progressively higher fields. Concave-up curvature implies an inhibited rotation of positively magnetized domains as negative domains are magnetized. This onset of oppositely coupled magnetization creates an asymmetric hysteresis difference caused by a movable or changeable magnetic microstructure (described in detail by Robinson *et al*. 2012b, their fig. 10). Present results imply that, as a greater proportion of self-reversed magnetization is established with falling T, there is a large increase in the potential for magnetic microstructures that need to be moved against the force of normal antiferromagnetic interface interactions, in order to establish positive magnetization. The magnetic microstructures create a higher resistance to saturation.

Similar loops are given by Lagroix *et al*. (2004, their fig. 2) for their $X = 0.70$ samples Q1300 and Q1050 (see above) at 170, 150, 110–115, 90 and 30 °C. Their 170 °C and 150 °C loops are similar to our 280 °C loop. Their lower T loops show an increasing importance of ferrimagnetism, but none of the loops shows the regions of increasing slope, that we attribute to microstructures with increasing resistance to saturation, shown by our $X = 0.60$ sample B-06. In our range of experiments this property is found only in samples of composition $X = 0.60$, and not in $X = 0.65$ or 0.70. Likely chemical ordering is more sluggish for $X = 0.60$ than for

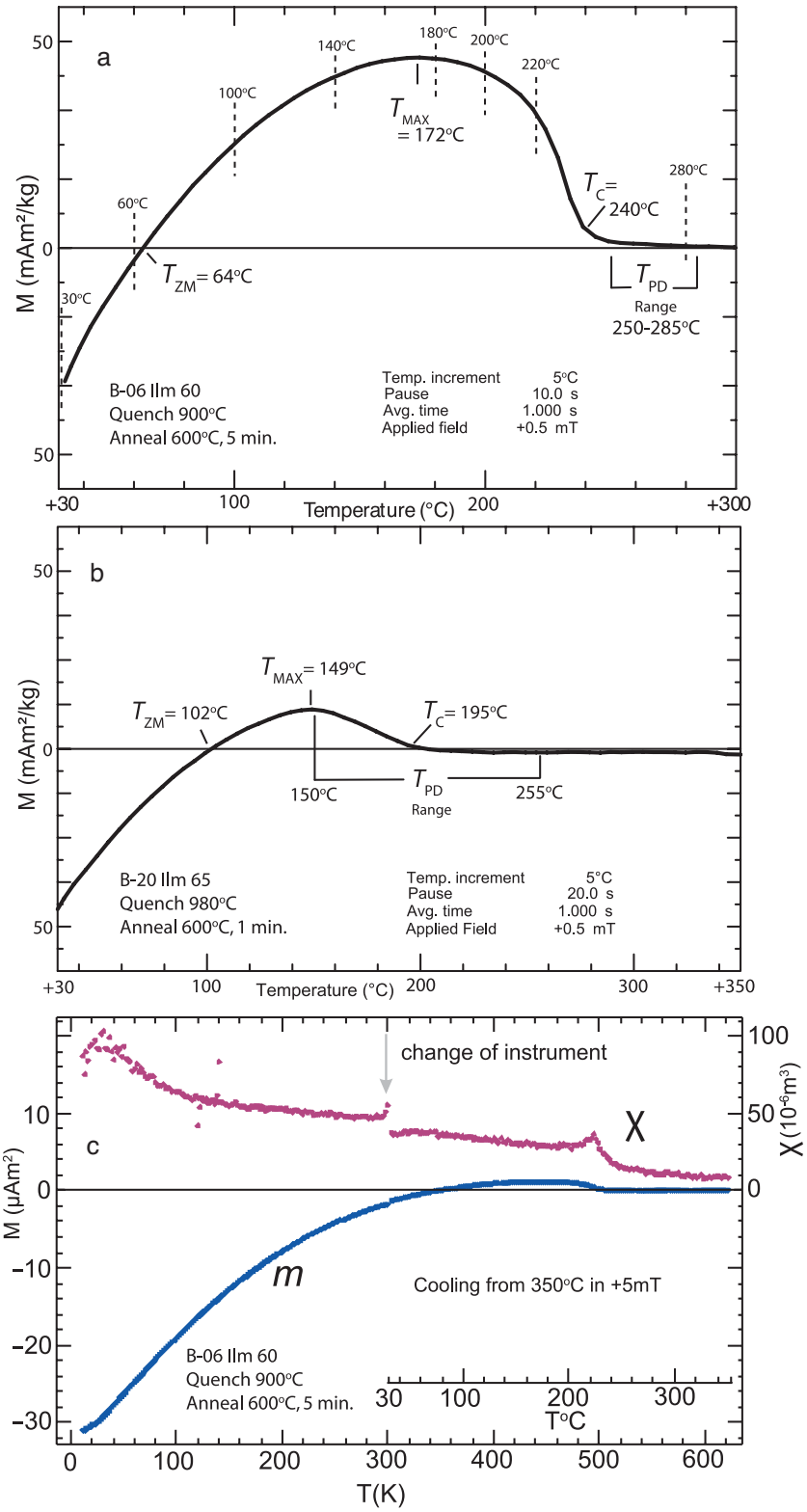

Figure 2. Results of cooling experiments on samples B-06 and B-20. Panels (a) and (b) show magnetic intensity in M ($Am^2\ kg^{-1}$), measured in a field of 0.5 mT, beginning at 350 °C with measurement increments of 5 °C after 10 or 20 s pauses. Intensity includes both remanence and induced magnetization from the weak positive field. The latter adds a small positive component to the magnetization, but curve shape is mainly controlled by remanence. See text for explanation of T_{PD}, T_C, T_{MAX} and T_{ZM}. Panel (a) shows temperatures of hysteresis loops in Fig. 3. Panel (c) shows results of a different cooling experiment on B-06 in which susceptibility and remanence were determined independently by stepwise cooling from 350 °C down to 10 K in steps of 2 K, using two different instruments. At each step a magnetization curve from $H = 0$ to 5 mT was measured as explained in the text.

more Ti-rich compositions, so that magnetically significant quench microstructures are more easily formed and less easily annealed away. We suspect that this property of hysteresis loops may be found for some Ilm 65 and 70 samples, when run below RT, where there would be a greater proportion of self-reversed magnetization.

2.4 Analysis of high-*T* measurements of susceptibility and remanence

In connection with the cooling curve (Fig. 2a) and thermal hysteresis loops (Fig. 3) for sample B-06, an analysis was made of the measurements of magnetic susceptibility and remanence in Fig. 2(c) in the T range 350–200 °C. Fig. 4(a) shows inverse susceptibility versus T. Because the Curie–Weiss law predicts a linear slope of $1/\chi$ at high temperature, we interpret the observed curved behaviour as an effect of variable composition and approximate it by three different slopes. The changes in slope at ∼290 and ∼245 °C correspond approximately to the upper and lower limits of the T_{PD} range as shown in Fig. 1(a). The susceptibility peak indicates the predominant Curie T at 222 °C, ∼18 °C lower than T_C marked at 240 °C on Fig. 2(a), which, based on total magnetization, is biased towards the upper end of the Curie T spectrum in the mixture. Fig. 4(b) shows remanence. The onset of remanence acquisition, initially very weak, corresponds to the upper limit of the T_{PD} range at ∼285 °C.

2.5 Monte Carlo simulation of microstructure and cooling curve

The chemical and magnetic properties of rapidly cooled ferri-ilmenite solid solutions have been investigated extensively using atomistic computer simulations (Harrison *et al*. 2005; Harrison 2006; Robinson *et al*. 2012a). Cooling through the $R\bar{3}c$ to $R\bar{3}$ phase transition leads to the formation of fine-scale cation-ordered domains. Adjacent domains have an antiphase relationship with each other; an Fe-rich layer becomes a Ti-rich layer on crossing the domain boundary, and vice versa. In order to highlight this relationship, domains and their boundaries are referred to as APDs and APBs, respectively. Fig. 5 shows the results of a Monte Carlo simulation of a 48-layer supercell of Ilm 70, containing two APBs (Harrison 2006). The degree of cation order is defined by the order parameter:

$$Q = \frac{N_{\mathrm{Ti}}^{\mathrm{B}} - N_{\mathrm{Ti}}^{\mathrm{A}}}{N_{\mathrm{Ti}}^{\mathrm{A}} + N_{\mathrm{Ti}}^{\mathrm{B}}},$$

where $N_{\mathrm{Ti}}^{\mathrm{A}}$ and $N_{\mathrm{Ti}}^{\mathrm{B}}$ are the number of Ti^{4+} cations on A and B layers, respectively. Q can vary continuously from 0 to ±1, with $Q = 0$ representing a fully disordered state, and $Q = 1$ and –1 representing fully ordered and fully anti-ordered states, respectively. Fig. 5(a) shows the variation in Q throughout the simulation cell. Normally Q is considered in relation to two adjacent layers, and is not normally calculated for a single layer. However, magnetic interactions in each central layer take place mainly with half the atoms in the two neighbouring layers, thus achieving a total of two layers, from which a Q representing each layer can be calculated. On the left (cation layers 0–18) is an ordered domain with a high degree of cation order with Q approaching 0.9. On the right (cation layers 20–44) is an anti-ordered domain with Q approaching –0.75. APBs occur as Q passes through 0. During the chemical simulation at high T, the well ordered domain grows at the expense of the less well ordered domain, as shown by the arrows in Fig. 5(a). The corresponding variation in chemical composition throughout the simulation supercell is shown in Fig. 5(b). Again, as with Q, the values are averages between each central layer and half the atoms in the adjacent layers. Thus, a sawtooth pattern, as one would expect to see with alternating Ti- and Fe-rich individual layers, is not seen. The growing Ti-rich A-ordered domain on average reaches $X = 0.80$, whereas the shrinking Fe-rich B-anti-ordered domain reaches $X = 0.68$–0.64. Antiphase boundaries are Fe-enriched reaching $X = 0.57$. Fig. 5(c) shows the temperature dependence of the spontaneous magnetization of the simulation during cooling. All chemical changes occur at Ts above 350 °C, so the details of the cooling curve reflect the presence of compositions and microstructures produced outside the figure. The simulation compares favourably with the experimental observations (Figs 2a and b). Magnetic order first develops on cooling in the Fe-rich APBs. Given the disordered nature of the APBs, they are nearly antiferromagnetic and do not contribute greatly to the net moment. Magnetic order spreads on further cooling into the B-ordered domain that was shrinking. The low degree of cation order in this shrunken domain gives rise to a small positive net moment. As magnetic order spreads with further cooling into the A-ordered domain that was growing, the net ferrimagnetic moment decreases and eventually fully reverses. The origin of the reversal can be seen in the layer-by-layer spin profile obtained at 25 K in Fig. 5d). Positive and negative values alternate throughout the model in perfect antiferromagnetic interaction, even though the net magnetic moment is negative to the left and positive to the right across a chemical APB. Due to the antiphase relationship between adjacent domains, the ferrimagnetic moment of the well ordered A-domain is antiparallel to that of the less well ordered B-domain and considerably larger in magnitude. This illustrates a magnetically compatible p-domain in the terms of Robinson *et al*. (2012b) with no magnetic walls. Application of a strong magnetic field, causing reversal of the net moment in part of the model, would create a magnetic q-domain and a magnetic wall. Because of the Ilm 70 bulk composition, as well as different microstructure, as compared to Ilm 60 and Ilm 65 in Figs 2(a) and (b), full negative magnetization (T_{ZM}) is not attained until $T < 0$ °C.

2.6 TEM observations

We were unsure about possible thermal effects on degree of order caused by ion-thinning techniques used in preparation for TEM observations. For this reason only crushed grains mounted on grids were used, with consequent uncertainty about grain thickness, in turn relating to interpretation.

Results of TEM observations on samples B-06 and 20 are shown Fig. 6. Panel (a) of each shows a dark-field image taken through the 003 reflection of the Fe-Ti ordered phase. The intensity observed in the dark-field image is proportional to the local value of Q^2 integrated through the thickness of the sample. Hence it is not possible to distinguish between ordered ($Q > 0$) and anti-ordered ($Q < 0$) domains. However, it is possible to see relative variations in the overall degree of cation order. Light areas are locations where a high degree of order exists throughout the thickness of the section. Dark areas are locations dominated by either poorly ordered or disordered domains with lower values of Q^2. Line (001) indicates the orientation of the (001) plane and shows that the dominant orientation of phase interfaces is at angles of 17–34 ° from (001) in sample 06, and at angles of 20–28 ° from (001) in sample 20. Panel (b) of each shows a similar dark field image at higher magnification. Maximum size of more-ordered domains is ∼4 nm in B-06, ∼7 nm in B-20. Panels (c) show diffraction patterns of the samples taken

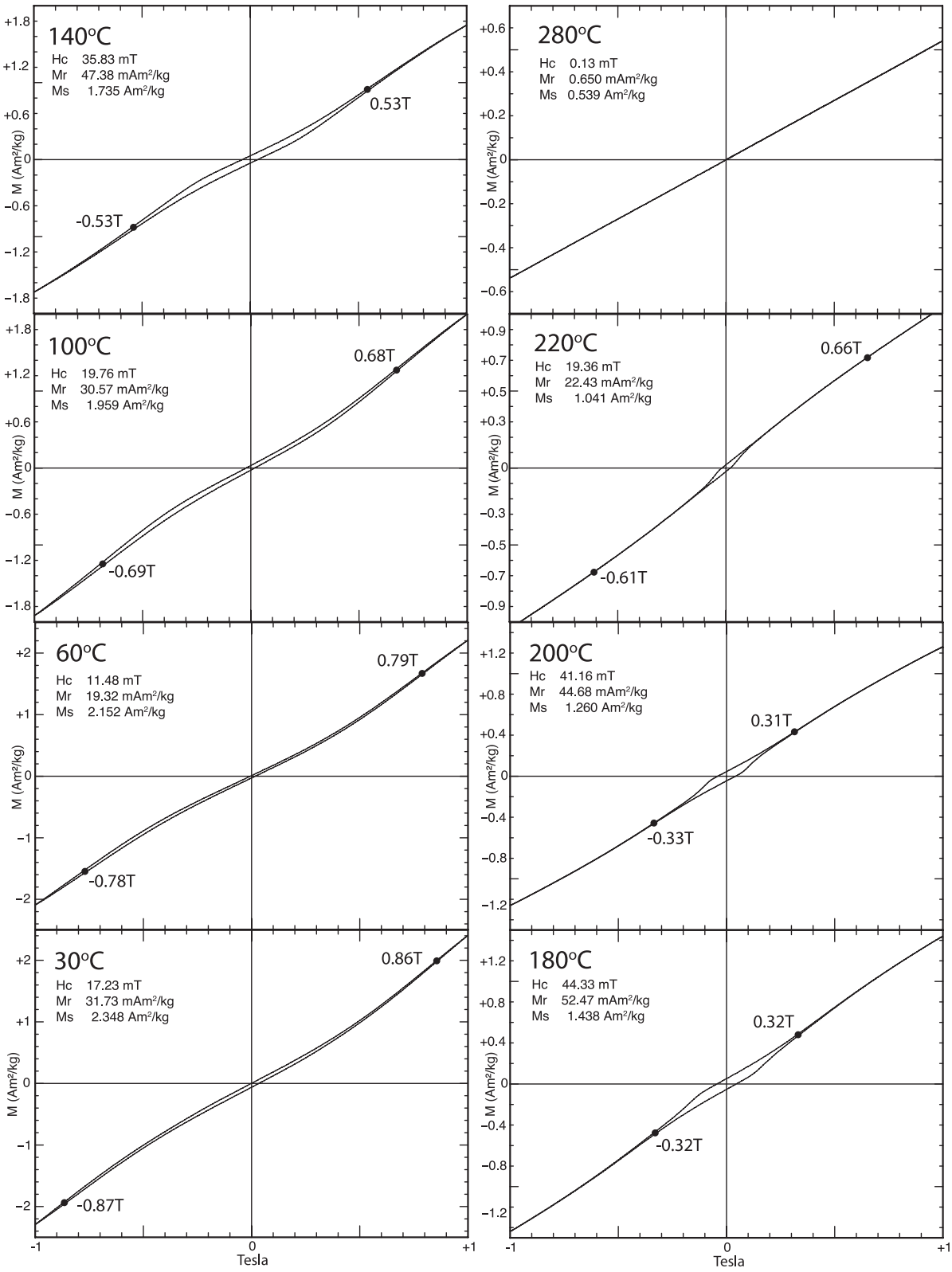

Figure 3. Hysteresis loops were measured on sample B-06 in a maximum field of 1 T after first heating to 350 °C, then cooling in a field of +0.5 T to 280 °C for the first loop, then cooling in absence of an applied field to *T*s of 220, 200, 180, 140, 100, 60 and 30 °C as indicated on Fig. 2(a). Dots and numbers indicate inflexion point locations in T calculated from average of lower and upper branches. The weight-normalized vertical scale is M (Am^2 kg^{-1}) and the horizontal scale is in T.

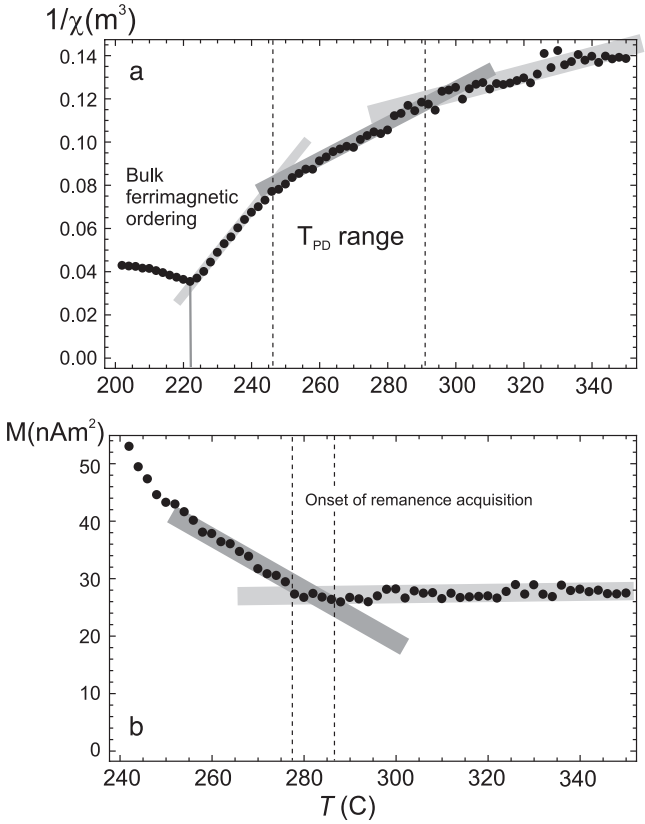

Figure 4. Results of thermal experiments on sample B-06 on cooling in fields of 0–5 mT in the range 360 to 240 °C. (a) Inverse susceptibility. Changes of slope ∼290 and ∼245 °C identify approximately the T_{PD} range shown in Fig. 1(a). Maximum susceptibility at 222 °C is where quantitatively significant ferrimagnetization is established, 18 °C lower than T_C as marked in Fig. 2(a). (b) Remanence. Onset of remanence acquisition corresponds to the upper limit of the T_{PD} range in Fig. 1.

with the electron beam parallel to the (110) zone axis with indexed reflections and orientations of the (001) plane. Panels (d) show enhanced images of a section of panel (a), outlined by dashed lines, emphasizing gradients between Fe-Ti ordered regions. The gradients have been calculated using a Gaussian gradient with two pixels radius. Darker colours indicate larger gradients. The grey scale has then been adjusted by changing contrast and brightness.

A general conclusion from TEM results is that these samples are dominated by a mixture of poorly ordered/disordered regions containing ordered domains of widely different sizes less than 4 and 7 nm, respectively. The TEM is incapable of detecting the difference between better ordered and better anti-ordered material, which likely occurs in roughly equal amounts overall. There may be locations where ordered and anti-ordered domains occur across anti-phase domain boundaries, however these cannot be distinguished here.

2.7 Significance of experiments, simulation and TEM

The magnetic experiments are presented in a general way to understand the chemical and magnetic background that could lead to conditions providing the four different temperatures discussed above. Initially this involves the exploration of the detailed chemical make-up of the APBs, because that chemistry, all created during quench and annealing at high T, is what determines the ultimate magnetization Ts involved in the magnetic experiments. Key insights into that chemistry provided by the Monte Carlo simulations of Harrison (2006) were known but not fully appreciated until recently. Some of the magnetic data, coupled with the TEM, can be used to make estimates of the composition distribution within the quenched and annealed samples. Samples with different thermal histories provide rather large variations in the detailed magnetic results. These will be explored in detail in later articles, but many exhibit most of the features discussed above. The TEM images of the two samples, suggest that at least these two consist dominantly of poorly ordered/disordered material with low Q values embedded with small ordered and anti-ordered domains of different sizes with higher Q values. It is impossible to prove or disprove the presence of anti-phase domain boundaries, which are significant, but not required for self-reversed thermoremanent magnetization.

3 COMPOSITION WAVES NEAR APBs: RELATION TO ACQUISITION OF SELF-REVERSED THERMOREMANENT MAGNETIZATION

3.1 Keys to chemical evolution

The introduction referred to earlier theoretical studies concerning chemical evolution during quench and annealing. We now understand that these provide the key to the high- T 'pre-destination T' and other features in the thermal experiments. Rather than expand further on the theory here, we give an intuitive and practical example of a chemical model that predicts magnetic results in reasonable agreement with the experiments.

3.2 Conceptual chemical model of phase interface region

Fig. 7 shows a sequence of thirty rhombohedral Fe-Ti oxide layers with various compositions and Q values, where Q is the Ti order parameter $(Ti_A - Ti_B)/(Ti_A + Ti_B)$ ranging from +1 (perfect order) through 0 (perfect disorder) to –1 (perfect anti-order).[1]

When the compositions of all layers are averaged, the result is exactly Ilm 60. To the left (pink layers 1–10) is a region of ordered ferri-ilmenite in the composition range Ilm 50–57.5 and $Q = +0.20$ to 0.60, within a domain that has undergone Fe-enrichment relative to the initial bulk Ilm 60. The ferrimagnetic moment of these layers is determined by the difference in magnetic moments (here calculated ideally at 0 K) between Fe^{2+} ions in the Fe layers and Fe^{2+} ions in the Ti layers, which ranges from +0.40 to +1.38 Bohr magnetons (μB) per formula unit (pfu). Note that Ilm content, Q value, and net magnetic moment all decrease approaching the phase boundary. Next to the right, in succession occur a contact layer (11, red-orange), two disordered layers (12,13, yellow), and a second contact layer (14, violet) that constitute the key parts of an anti-phase boundary between A-ordered and B-anti-ordered regions. These are consistent with previous models (Robinson *et al*. 2012a) indicating that a contact layer has a composition that is an average of a disordered layer and the nearest Fe-layer in the adjacent ordered phase. Contact layer 11 has composition $Ti_{0.225}\ Fe^{2+}{}_{0.275}\ Fe^{3+}{}_{0.50}$, and a net moment with the adjacent disordered layer of +0.1 μB. Contact layer 14 has composition $Ti_{0.21125}\ Fe^{2+}{}_{0.32625}\ Fe^{3+}{}_{0.4625}$, and

[1] The use of A and B here is traditional to refer to the first and second layer of a consistently ordered multilayer sequence. Unfortunately, this can be confused with a different traditional terminology for A-ordered and B-anti-ordered regions where A and B have a different meaning.

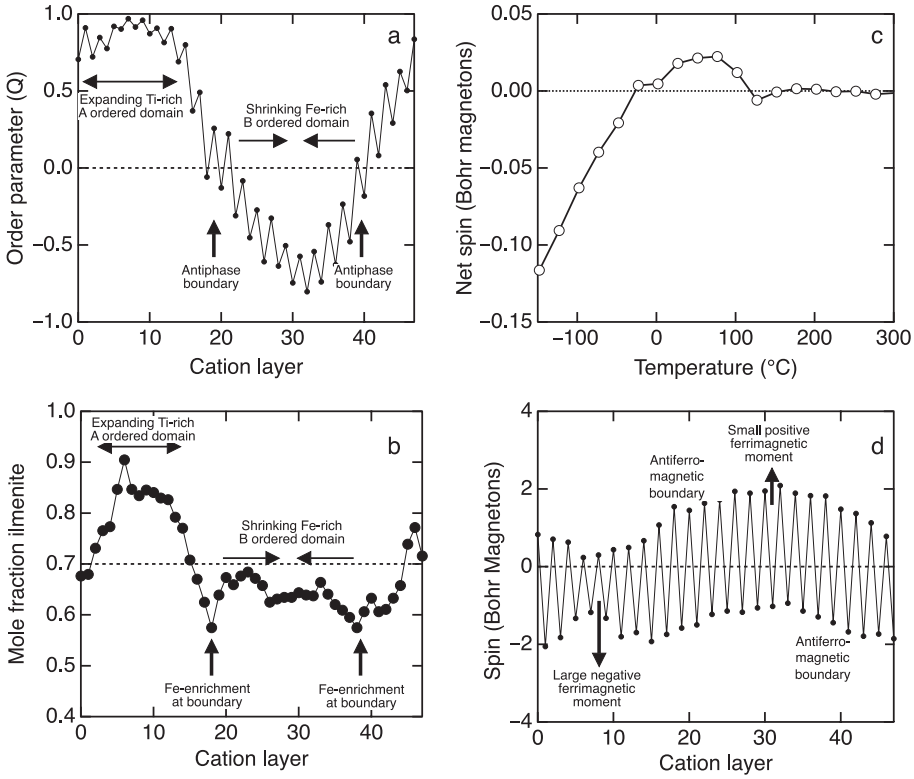

Figure 5. Results of a Monte Carlo simulation originally described by Harrison (2006) using a model 48-layer supercell of composition of Ilm 70, cooled through the R-3C to R-3 Fe-Ti ordering transition. When stopped, the simulation had produced a growing Ti-rich A-ordered domain and a shrinking Fe-rich B-anti-ordered domain separated by two antiphase boundaries. (a) Record of calculated Q values for the 48 layers. (b) Record of calculated X Ilm for the 48 layers. (c) Synthetic magnetic cooling curve for the arrested Monte Carlo chemical simulation. (d) Magnetic spin in Bohr magnetons modelled at 25 K for each of the 48 layers. These are not averages as in (a) and (b) but individual layer values.

a net moment with the adjacent disordered layer of –0.1175 μB. Because the contact layers have higher Fe content than the disordered layers, the mean interlayer Fe count registered in the upper part of Fig. 7 is the highest in the model.

To the right of the APB, the model now moves into a (blue) region of Fe depletion. Here we assumed that, during APB motion, the Fe-depletion is greatest away from the APB, where ordering was initiated, and is progressively less as the APB is approached, marked by rising Fe total in the layers. Q values are most negative (most anti-ordered) away from the boundary and approach zero towards the boundary. The layers range in composition from Ilm 57.5 to Ilm 70 with Q values decreasing from −0.40 to −0.80, and net magnetic moments at 0 K from –0.92 to –2.24. Note that this ordered domain, having a higher average degree of cation order, would appear lighter than the one on the left in a dark-field TEM image taken with the 003 reflection (Fig. 6). We considered a slightly different model in which the most Fe-impoverished layers form a moat adjacent to the APB, but do not discuss it here. In both progressions away from the APB, composition changes lower the Curie Ts, but increase the absolute magnetizations, while increasing Q values also increase the magnetizations.

We pause here to point out that the contact layer concept, strongly supported by studies of true exsolution between near-end-member hematite and ilmenite, is not an absolute requirement here. Indeed, one may question how a single atomic layer might contain enough atoms to achieve an average randomly chosen intermediate composition. The presence or absence of contact layers is not a serious issue when it comes to the magnetic effects of Fe-enriched composition waves with low or no chemical order. If one accepts contact layers, as in Fig. 7, then the theoretical minimum thickness for an APB is four atomic layers or ∼0.9 nm.

Overall, as illustrated by total Fe content in the upper part of Fig. 7, the composition profile has the shape of a breaking wave, with, however, the steep side in the direction of retreat rather than advance, as with a wave approaching a beach. Assuming that the chemical profile shown here can be obtained by the proposed mechanisms during quench, with or without annealing, we trace the progressive thermal magnetization, magnetic coupling and theoretical progress of magnetic moments within the model.

3.3 Magnetization *T*s

To a first approximation, magnetization Ts in the hematite-ilmenite series are proportional to the total amounts of Fe^{2+} and Fe^{3+} in the alternating layers, where the theoretical magnetic moments at 0 K are 4 and 5 μB, respectively. The top chart in Fig. 7 shows the averaged total Fe content for pairs of layers. The top line of compositions is for pairs having the same Fe^{3+} content; the lower line shows averages for pairs of layers with different Fe^{3+} contents. There is argument as to whether the magnetization T is slightly higher or lower in ordered phases as compared to the disordered phases. Taken together, the common results lie on a nearly straight line (Ishikawa & Akimoto 1957), where order could produce differences of only 2–5 °. With this understanding, we assign magnetization Ts to each of the parts of Fig. 7. Derived magnetization Ts for several compositions are marked on the right-hand side, and all are indicated in Fig. 8(a).

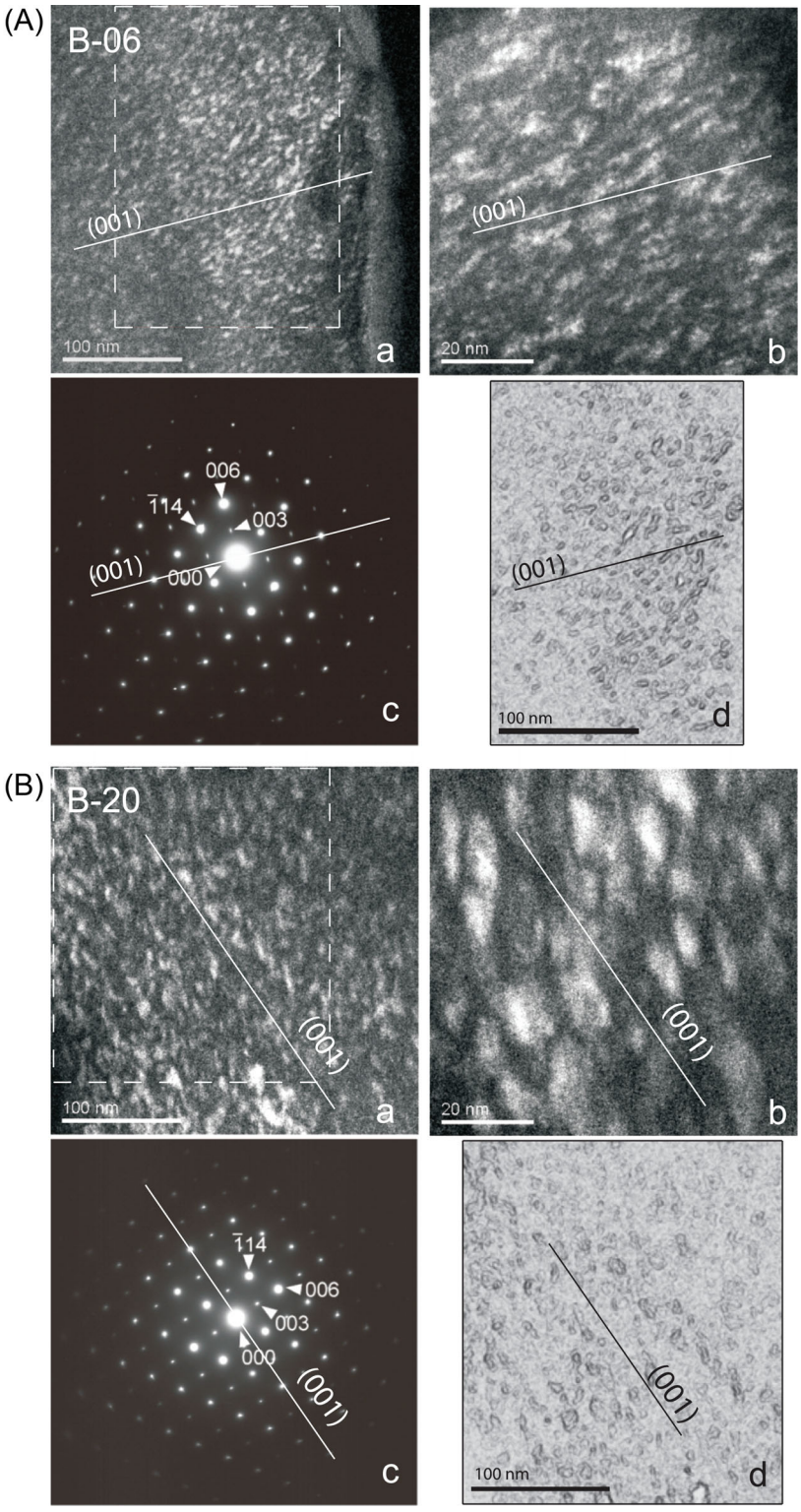

Figure 6. Results of TEM investigations on B-06 (A) and B-20 (B). Panels (a) show dark field TEM images taken through the 003 reflection of the Fe-Ti ordered phase. Panels (b) show similar dark field images at higher magnification. Panels (c) show diffraction patterns, indexed reflections and orientations of (001) plane. Panels (d) show enhanced images of parts of (a) outlined by dashed lines emphasizing gradients between Fe-Ti ordered regions.

3.4 Theoretical thermal magnetization profile

The magnetization *T*s and theoretical magnetic moments of pairs of layers, are charted in Fig. 8(a). The intensities used take no account of the actual thermal effects on intensity, but are based on the theoretical values of magnetic moment at 0 K, expressed as Bohr magnetons. Fig. 8(a) has only a qualitative relationship to the cooling curves of Figs 2(a) and (b). The effects of *T* in reducing intensity between absolute zero and the Curie *T*s for each

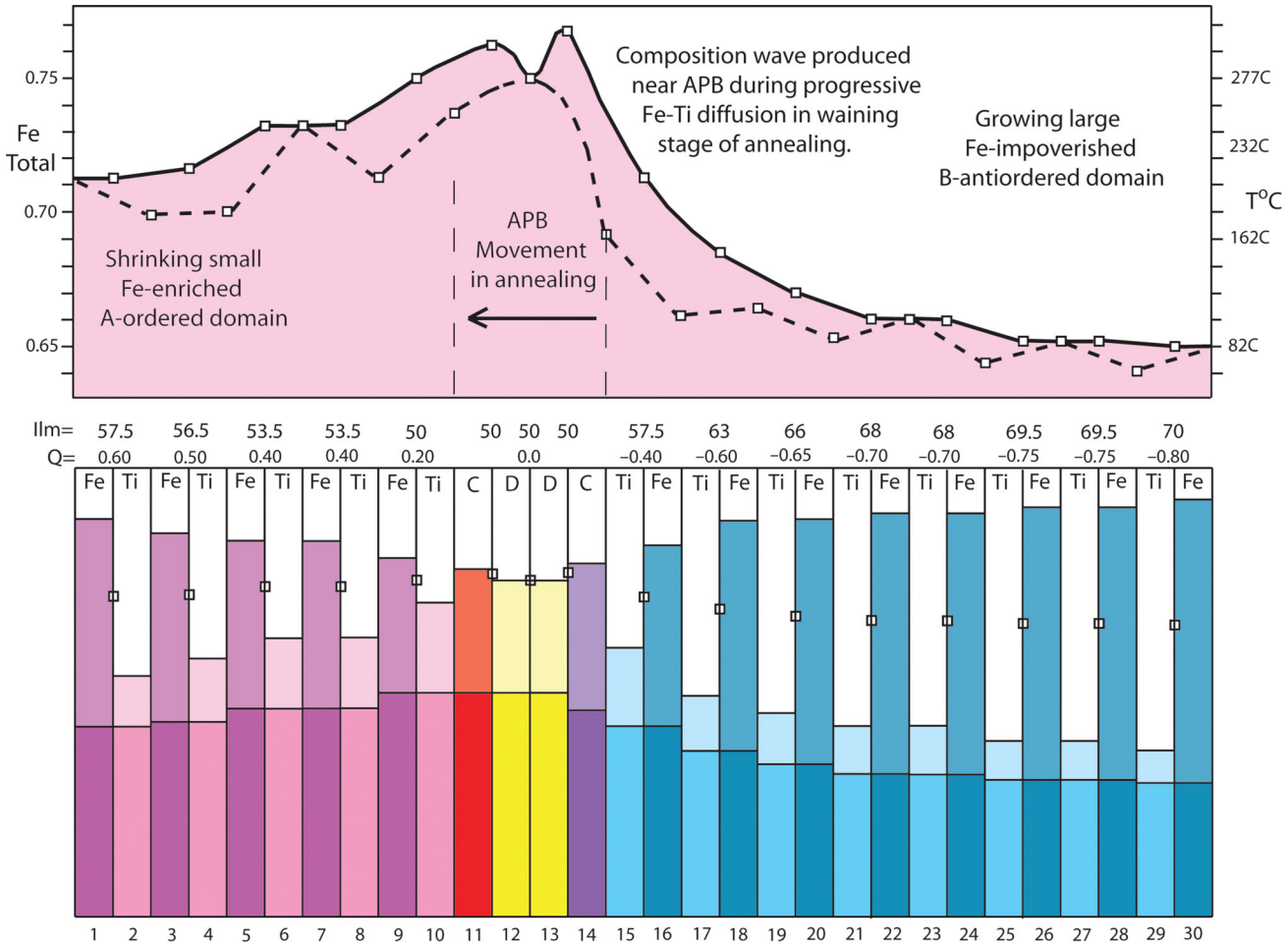

Figure 7. Thirty-layer model of the interface between a shrinking small Fe-rich ordered domain to the left (pink layers) with positive Q values, and a growing large Fe-impoverished B-anti-ordered domain to right (blue layers) with negative Q values, separated in the centre by contact layers and two disordered layers (yellow). Each layer composition column shows the Fe^{3+} content at the bottom, then the Fe^{2+} content, with Ti content represented by white at the top. Fe^{2+} layers are shaded darker than Ti layers. Fe^{2+} and Ti content of layers is allocated according to Q value. The graph at the top charts the average total Fe contents of all pairs of layers, illustrating the shape of the resulting asymmetric composition wave. The movement direction of the wave during arrested chemical evolution is indicated.

composition are modelled in Fig. 8(b), based on a theoretical curve of magnetic intensity versus T for hematite (Harrison 2006).

The initial magnetization in a weak positive field takes place at 277 °C for the Ilm 50 compositions of the two disordered layers, the two contact layers and two layers of weakly ordered Ilm 50 with $Q = +0.20$ on the APB. The net magnetizations of these (expressed as ferrimagnets in μB) are 0, +0.1, –0.1175 and +0.4, respectively, giving a net moment +0.3825. At this T contact layers on both sides of the APB are magnetized with + and – magnetizations, and these magnetizations provide the local 'pre-destiny' for all that is to follow, even though the initial magnetizations are very weak. To the left-hand side in Fig. 7 there follow one four-layer step, and one two-layer step with Ts, compositions, Q values, magnetizations and progressive magnetic sums: 246 °C, Ilm 53.5, $Q = +0.40$, +1.7136 μB, +2.0961 μB; and 217 °C, Ilm 56.5, $Q = +0.50$, +1.1304 μB, +3.2265. The last step to the left at 205 °C involves two layers Ilm 57.5, $Q = +0.60$, +1.38 μB, and, to the right, two layers Ilm 57.5, $Q = –0.40$ and –0.92 μB, giving a magnetic sum of +3.6865 μB. Charted magnetization begins to drop beyond this point. Note that the total theoretical magnetization here is already composed of dominant positive components, and also a negative component. Beyond this there is no further composition to add to the positive magnetization from layers to the left of the APB in Fig. 7, and all additional magnetization is from progressive negative magnetization from layers on the right side of the APB.

Next are two two-layer steps and one four layer step, with Ts, compositions, Q values, magnetizations and cumulative magnetizations as follows: 150 °C, Ilm 63, $Q = –0.60$, –1.512 μB, +2.1745 μB; and 124 °C, Ilm 66, $Q = –0.65$, –1.716 μB, +0.4585 μB; 105 °C, Ilm 68, $Q = –0.70$, –3.808 μB, –3.3495 μB. Here, for the first time, there is a net negative self-reversed magnetization, suggesting a 'T_{ZM}' on the chart near 120 °C. An additional four-layer step and one two-layer step with Ts, compositions, Q values, magnetizations and cumulative magnetizations are as follows: 87 °C, Ilm 69.5, $Q = –0.75$, –4.17 μB, –7.5195 μB; 82 °C, Ilm 70, $Q = –0.80$, –2.24 μB, –9.7595 μB.

In this theoretical chart all layers are now magnetized and no further changes are possible, but in real magnetic experiments, falling T has magnetic effects far below the theoretical Curie T. Considering these limitations, this simple conceptual magnetic model, involving only a few layers, compared to millions in the real material, provides a remarkably good template to understand what has actually happened in these experiments.

Table 1. Layer compositions, Q values, magnetization temperatures and magnetic moments portrayed in Figs 7, 8(a) and (b).

Fig. 7 Layer Numbers	Fig. 7 Comp. (X)	Fig. 7 Q	Fig. 8A Mag. T°C	Fig. 8A Mag. μB at 0 K	Fig. 8A Cum. Mag. μB at 0 K	Fig. 8B Cumulative Mag. μB at T	Fig. 8B Comment
11-12	*0.50*	*x*	*277*	*+0.1*			
13-14	*0.50*	*x*	*277*	*–0.1175*			
10-9	*0.50*	*0.20*	*277*	*+0.4*			
Total			**277**	**+0.3825**	**+0.3825**	**0.0**	T_{PD} = 277°C
14-9			261			+0.0318	**A-domain magnetization**
8-7-6-5	0.535	0.40	246	+1.7136	+2.0961	+0.0918	
14-5			230			+0.3175	
							T_C
4-3	0.565	0.50	217	+1.1304	+3.2265	+0.6152	~225°C
2-1	*0.575*	*0.60*	*205*	*+1.38*			Initial reversed magnetization
15-16	*0.575*	*–0.40*	*205*	*–0.92*			
Total			**205**	**+0.46**	**+3.6865**	**+0.8845**	
16-1			178			+1.6056	**B-domain magnetization**
17-18	0.63	–0.60	150	–1.512	+2.1745	+2.0548	
18-1			137			+2.0571	T_{MAX} = 140°C
19-20	0.66	–0.65	124	–1.716	+0.4585	+1.8989	
21-24	0.68	–0.70	105	–3.808	–3.3495	+1.3637	
25-28	0.695	–0.75	87	–4.17	–7.5195	+0.1624	T_{ZM} = 85°C
29-30	0.70	–0.80	82	–2.24	–9.7595	–0.2109	
30-1			74			–1.2742	
30-1			66			–2.1709	
30-1			58			–3.0708	
30-1			50			–3.9080	
30-1			25			–5.2562	
30-1			0			–6.2275	

The template for progressive magnetization of Fig. 8(a) is developed in Fig. 8(b) to reflect the fact that magnetizations are negligible near the respective Curie Ts, then ramp up rapidly, and then rise more slowly until reaching the theoretical maximum value at 0 K. The thermal profile used in estimating this progress of total magnetic intensity with falling T is one based on hematite (Harrison 2006). The resulting thermal curve is better at matching the character of the experimental cooling curves of Figs 2(a) and (b), with a T_{PD} at 277 °C, $T_C \sim 220$ °C, $T_{MAX} \sim 140$ °C and T_{ZM} at 85 °C. Although the experimental cooling curves are measured in a positive inducing field of 0.5 mT, and the induced magnetization contributes positively to the total magnetization, it does little to change the shapes of the curves, which are controlled by the abundances of the layers in any model and the details of how the remanence is acquired.

The upward concavity of the theoretical magnetization curve at low T compared to the striking downward concavity in the experimental curves of Figs 2(a)–(c) points to a common property of interfaces in these materials. This downward concavity in the experiments may suggest that some layers that acquire a positive magnetization at higher T, are forced at progressively lower Ts into self-reversal by material adjacent to APBs. It should be possible to incorporate this into a layer model, but perhaps not one with so few layers. We also have no control on the T and domain sizes by which such theoretical 'forced self-reversal' might occur.

Table 1 provides a list of the layers in Fig. 7 with their compositions, Q values, T_C and theoretical magnetizations at 0 K. It also provides the cumulative magnetic moments based on 0 K as in Fig. 8(a), and cumulative moments based on a thermal model as in Fig. 8(b). Finally, comments are provided linking the synthetic cooling curve Fig. 8(b) with the real cooling curves of Figs 2(a) and (b).

3.5 Summary of progressive magnetization of Fig. 7 as illustrated in Fig. 8(b)

(1) Fe-rich compositions near Ilm 50 (including weakly ordered material) mark the onset of magnetization at high T—the pre-destination point. Near this, in a positive magnetic field, the Fe-rich side of the APB acquires a positive magnetization, leading to progressive positive magnetization of the adjacent Fe-enriched domain, but a weak negative magnetization is also acquired on the Fe-impoverished B-anti-ordered domain side. Note that in the simple profile of Fig. 8(b) all pre-destination takes place below one T of 277 °C. This differs strikingly from the TPD range in experimental samples, reflecting the fact that the chemical waves in experimental samples are not of uniform height or composition range. In the

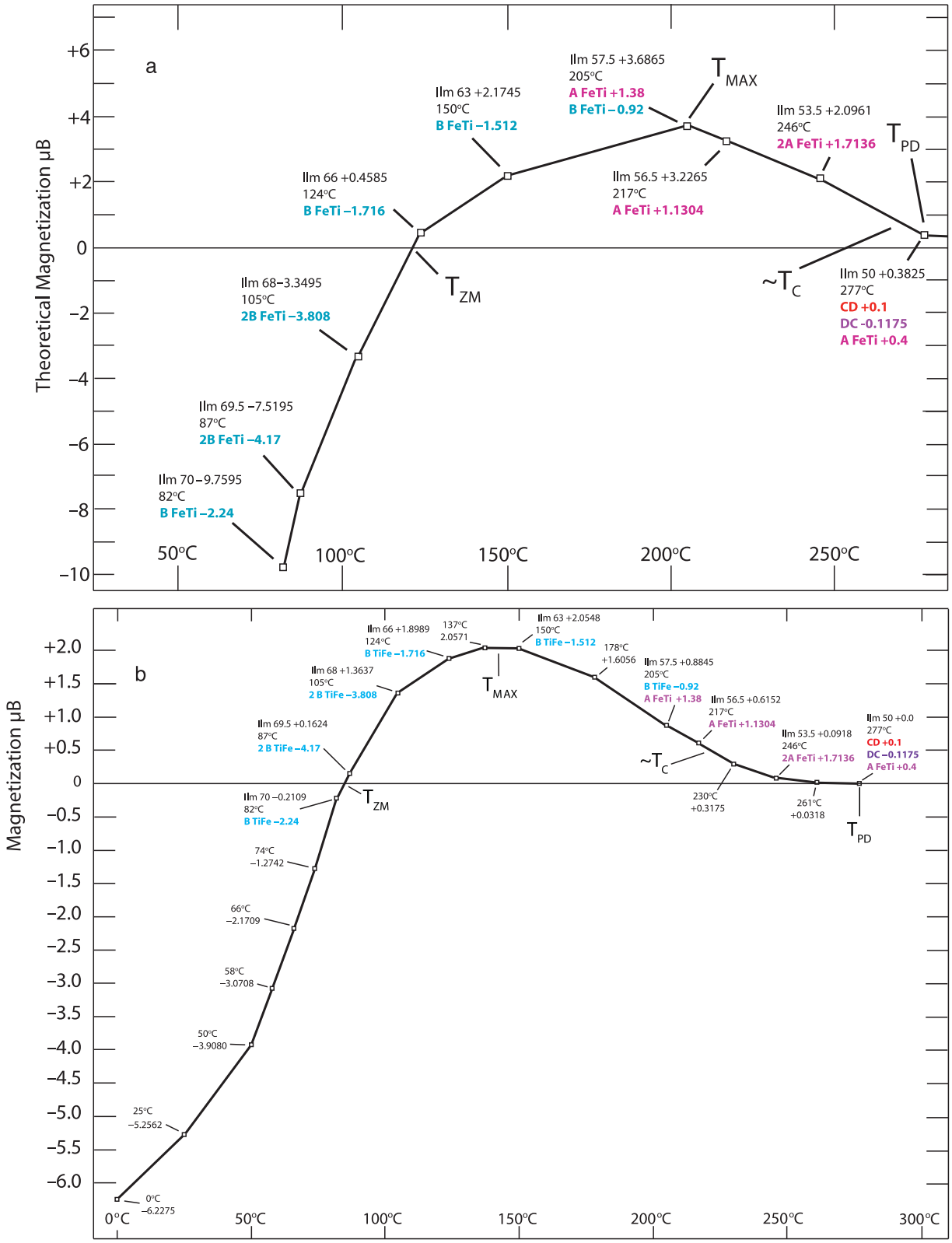

Figure 8. (a) Chart showing progressive magnetic acquisition *T*s of the layers in Fig. 7, magnetic moments of constituent pairs of layers calculated at 0 K, and cumulative net magnetic moments of the layers as the magnetization *T*s are reached with falling *T*. The layer magnetic moments are colour coded according to their general colours in Fig. 7. This is not a cooling curve because magnetic moments calculated at 0 K are represented as applying at the Curie *T*. (b) Synthetic cooling curve for the layer model of Fig. 7. Colour coding of calculated moments the same as in (a). Magnetic intensity for each layer is calculated in terms of a magnetic fraction based on the thermal difference at any temperature between the Curie *T* of the layer and 0 K. This magnetic fraction is 0 at the Curie *T* and reaches 1.0 at 0 K. The layers of Fig. 7 provide only a single T_{PD}, not a range, which would involve more varied wave chemistry as suggested for Figs 2(a) and (b). T_C, T_{MAX} and T_{FR} have similar significance as in Figs 2(a) and (b).

samples, one probably needs to be thinking in terms of 'blocking' rather than simply assuming that stable remanence is acquired immediately on cooling below Curie *T*s of regions only a few layers thick. The blocked Fe-rich '*x*-phase' is identified as the crests of waves, and the range of T_{PD} may be due to a range of blocking temperatures due to variations in composition but also probably to variations in the width/connectivity of the Fe-rich crests.

(2) Positive magnetization expands through the Fe-rich A-ordered domain in compositions Ilm 53.5–57.5 until it is all magnetized below 205 °C. Near this *T*, negative magnetization also begins to grow in layers within the B-anti-ordered domain with Ilm 57.5 composition. Initially this negative magnetization is weak compared to the positive magnetization that began at higher temperature, but, with falling *T,* this makes a progressively larger share and magnetization of compositions Ilm 57.5 and Ilm 63 begin to take over at $T_{MAX} \sim 140$ °C.

(3) Additional negative magnetization is acquired in the Fe-poor B-anti-ordered domain in compositions from Ilm 66 to 70, with increasingly negative *Q* values. These strong negative contributions to magnetization grow, so that this net magnetization eventually dominates with falling *T*, passing 'T_{ZM}' at 85 °C, the temperature where net magnetization passes a value of zero.

3.6 Charge balance at phase interfaces

Earlier (Robinson *et al*. 2012a) we showed that there is charge imbalance at interfaces between ordered and anti-ordered phases of identical composition. This can be reduced but not eliminated by placing 'contact layers' at boundaries between disordered and ordered layers. This is particularly important when the ordered and anti-ordered layers are of uniform composition and have large *Q* values. When adjacent layers are of slightly different composition but of low *Q* value, imbalances are still there, but less significant, leading to questions about whether contact layers are needed. The simplest evaluation is given in Fig. 9. Here an interlayer positive charge of 6 is exactly correct to satisfy three oxygen cations, and

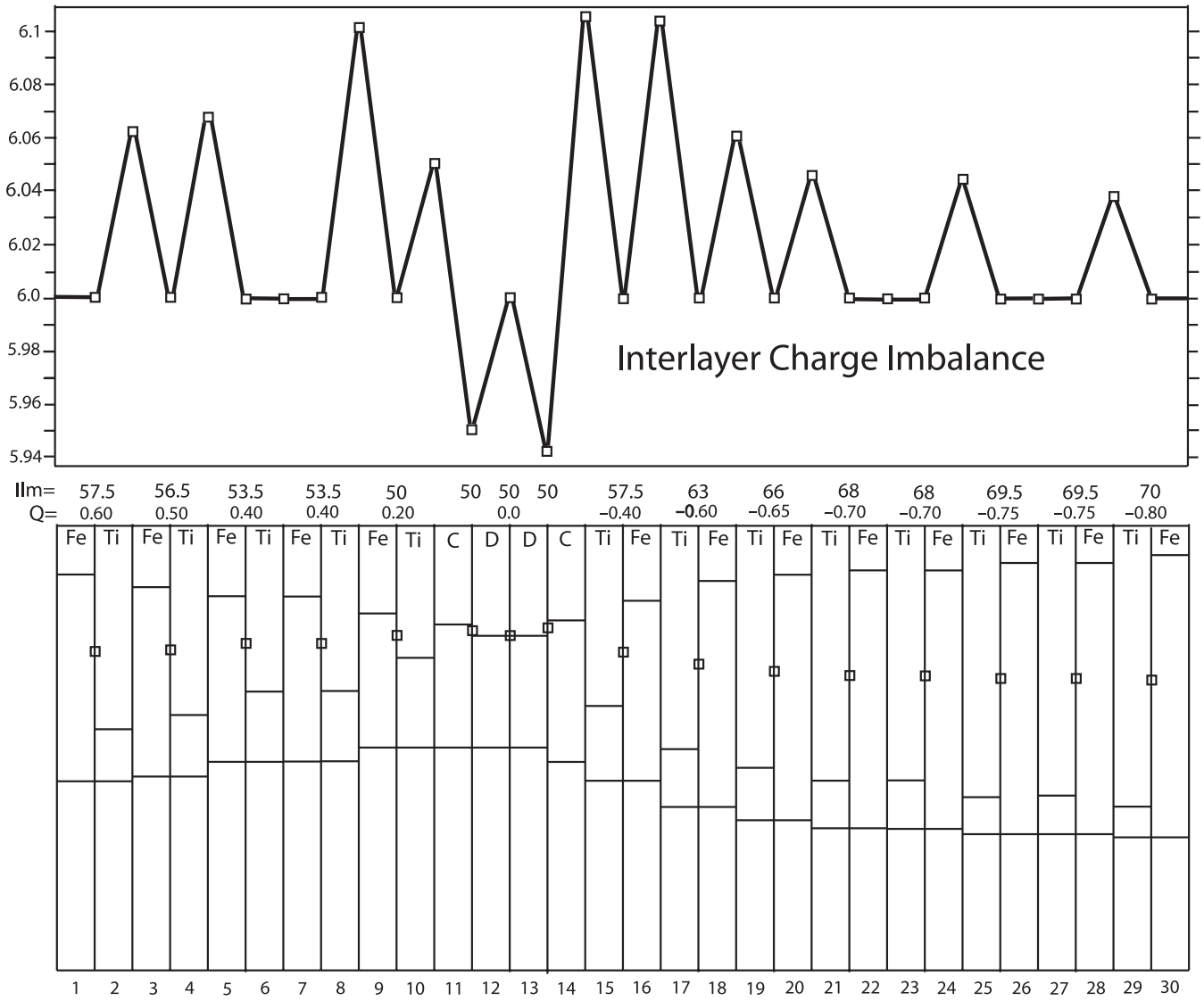

Figure 9. The same layer model as in Fig. 7, with charge balances plotted above it between every pair of layers, calculated as the average charge contribution to three oxygen in a formula unit. For any disordered or ordered pair of layers, the charge is 6.0, but for contacts between pairs of layers of different composition there is either an overcharge with values above 6, or an undercharge with values below 6. Evaluation was carried out using only simple bond strength without using bond valence (Robinson *et al*. 2006).

this value is achieved between layers in any ordered or disordered phase. However, it is not achieved at interfaces between phases of different composition, with mostly positive deviations up to 6.11, and negative deviations down to 5.94 associated with contact layers. We tested balances where contact layers are eliminated, placing disordered layers directly against either Ti layers or Fe layers of the adjacent phases. For disordered layers against Ti layers (TiD or DTi) the values are overcharged (6.1 and 6.115), for disordered layers against Fe layers (FeD or DFe) the values are greatly undercharged (5.9 and 5.89), suggesting that contact layers are still useful.

Fig. 9 suggests an interesting and not unexpected feature of APB regions, namely that achievement of perfect charge balance is not possible. This perhaps illustrates one aspect of the driving force to grow ordered domains and eliminate phase boundaries, namely to eliminate this inherent charge imbalance. Note that in the Monte Carlo simulation of Fig. 5 there is continuous variation in composition and Q value which would result in a more even distribution of charge imbalance than in the 'stepped pair' model of Fig. 7. Such continuous gradation may in fact occur in the natural material and could be the basis for a more sophisticated simulation than the conceptual model used here.

3.7 Discussion

The chemical model in Fig. 7 can account for magnetic events in some of our quenched and annealed samples, but certainly not all. Within the general principles outlined, there is room for chemical modifications to explain features found in some samples. In cooling curves on other samples with very similar shape, the magnetization passes 'T_{MAX}' indicating acquisition of some negative magnetization, but with continued falling temperature to 30 °C never passes 'T_{ZM}' to achieve net self-reversed magnetization.

This new conceptual model sheds significant light on the work of Nord & Lawson (1992), who understood antiferromagnetic coupling between ordered and anti-ordered phases (see their Fig. 12), but made little use of it. Despite those observations, they suggested that the key to magnetic self-reversal lay in the APBs, which they considered likely to be Fe-enriched. In our model, it is in fact the Fe-enriched domain boundaries with opposed magnetic moments, that provide the 'pre-destination' for magnetic self-reversal, whereas the bulk antiferromagnetic relationship and coupling between ordered and anti-ordered regions is what allows the self-reversed 'destiny' to be fulfilled!

4 THE CHEMICAL-WAVE CONCEPT WHERE ORDERED AND ANTI-ORDERED DOMAINS ARE EMBEDDED IN DISORDERED REGIONS

4.1 A two-wave model

An important step in textural evolution at high T towards a scenario with ordered and anti-ordered domains separated by antiphase boundaries, as illustrated in Fig. 7, is a situation where large and small ordered and anti-ordered regions lie completely enclosed in a disordered region. This was illustrated in articles II (Robinson *et al*. 2012a) and III (Robinson *et al*. 2012b). In the latter, it was proposed, with uncertainty that the smaller A-ordered and B-anti-ordered regions could magnetize at a higher temperature than the larger A-ordered and B-anti-ordered regions. The uncertainty was related to an earlier demonstration that Fe-enrichment of small regions can be related to the fact that these regions were 'shrinking' during overall coarsening. This could not be used to explain Fe-enrichment of small domains, which were 'growing' at the expense of a disordered host, and were small because their ordering began later than ordering in the larger domains. With the chemical wave concept in mind, as developed in Fig. 7, it seemed wise to explore this scenario at this less developed stage in chemical evolution.

Fig. 10 provides a theoretical profile across two phase boundaries involving 60 layers. In the centre (yellow) is a significant disordered region. On the left it is bordered by the edge of a small A-ordered domain (pink) that was growing during the time of arrested evolution, with a contact layer (red) on the boundary with the disordered phase. On the right-hand side, the disordered region is bordered by a large and growing B-anti-ordered domain (blue) with a contact layer (violet) on the boundary. The centre of the disordered domain is composed of layers of composition Ilm 60, representing the original disordered bulk composition. On the left, in the process of ordering in the A-ordered domain, Fe has been progressively depleted from the centre, and added to the boundary against the disordered region. Similarly, on the right, in the process of ordering the B-anti-ordered domain, Fe has been progressively depleted and added to the boundary against the disordered phase. In preparing this model, it was realized that the ordering on opposite sides of the model are completely independent. It is divided into two equal parts, layers 1–30 and 31–60. The average composition in both parts is Ilm 60. Among layers 1–30 there are more disordered layers and fewer ordered layers, and the Fe-enriched wave along the phase boundary is lower. Among layers 31–60 there are fewer disordered layers and more ordered layers, and the Fe-enriched wave along the phase boundary is higher. The two waves, of different heights, were in convergent motion during cooling. The progressive thermal magnetization of this model, including the concept of 'magnetic backwash' is covered below and summarized in Table 2.

4.2 Magnetization steps

Progressive magnetization of the two-wave model uses the same approach as with the single-wave model, with magnetization proceeding with falling T starting with the most Fe-rich compositions at Ilm 48 and ending with the most Fe-poor compositions at Ilm 70. These are not spelled out in such detail here, but summarized in the thermal acquisition profiles in Fig. 11 and in Table 2. The first part to magnetize in a positive field is the contact layer and adjacent disordered material (yellow layers 39–40–41 and violet layer 42) in the centre of the right hand wave, which would acquire a positive magnetization. The second feature to magnetize, also with a positive magnetization, would be the contact layer and adjacent disordered material (red layer 15 and yellow layers 16–17–18–19–20) in the left-hand wave, followed by progressive magnetization of the disordered region (yellow layers 21–36) between the contact layers. Because both contact layers are positively magnetized at this stage, a 180 ° magnetic domain wall would form somewhere in the middle of the disordered phase, because the two contact layers are magnetically incompatible. In the nomenclature of Robinson at al. (2012b) the red contact layer would be in a p-domain ('top layer in a series magnetized to right'), the violet contact layer in a q-domain ('top layer in a series magnetized to left'). Both of the contact layer magnetizations are very weak.

Upon completion of magnetization of the disordered domain, magnetization would next proceed in the small A-ordered region to the left (pink layers 1–14) until its completion. This would produce a strong positive magnetic moment completely compatible with the red contact layer (15). In the midst of that T interval, blue

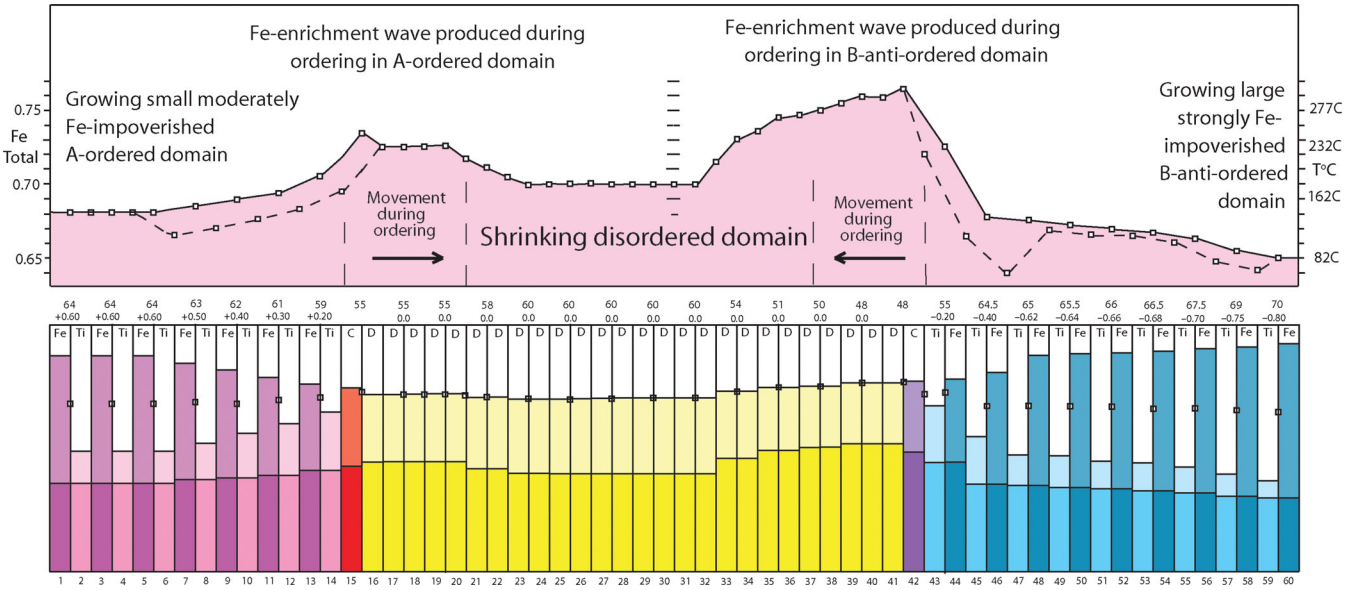

Figure 10. Sixty-layer model of the two interfaces where a small slowly growing Fe-rich ordered domain to the left (pink layers) with positive Q values, and a large rapidly growing Fe-impoverished B-anti-ordered domain to right (blue layers) with negative Q values, have both progressively impinged on a disordered central region (yellow) of the original disordered composition Ilm 60. System of graphing Fe^{3+} content, Fe^{2+} content, and Ti content is the same as in Fig. 7. Contact layers (15, red and 42, violet) occur at phase boundaries, but there are no anti-phase domain boundaries as in Fig. 7. Between the contact layers there are 26 disordered layers of slightly different composition. Left of red layer 11 (in pink) are the ferrimagnetic layers of the A-ordered domain progressing from Ilm 59 to 64 and in Q from 0.20 to 0.60. Right of violet layer 14 (in blue) are the ferrimagnetic layers of the B-anti-ordered region progressing from Ilm 55 to Ilm 70 and in Q from –0.20 to –0.80. In both progressions, composition changes lower the T_C, but increase the absolute magnetizations, while increasing Q values also increase the magnetizations. The graph at the top charts the average total Fe contents of all pairs of layers, and the shape of the two resulting asymmetric composition waves. Their movement directions before arrested chemical ordering are indicated.

layers 43–44 would also acquire a weak positive magnetization compatible with violet contact layer 42. We speculate that by this point, the strong positive magnetization on the left would drive the 180 ° purely magnetic wall in the antiferromagnetic disordered region far to the right until it overtakes the very weakly magnetized violet contact layer 42 as well as layers 43–44 on the right, which will then acquire a compatible negative remanence. As a result of this 'magnetic backwash', the scene is then set for the entire B-anti-ordered domain (blue layers 45–60) to acquire a negative remanence during further cooling. The 'backwash' effect is marked in Fig. 11(a) and in Table 2 by the change of the very weak magnetization of the violet contact layer 42 (Ilm 48 in Fig. 10) and blue layers 43–44 (Ilm 55 in Fig. 10) from positive to negative (note × 2 in Table 2). This would happen either before, or at the moment, when the positive magnetization of the left-hand A-ordered region is completed at 140 °C (T_{MAX}) in Fig. 11(a).

A discovery in the two-wave model of Fig. 10, is that it shows why the small ordered and anti-ordered domains could be more Fe-rich and therefore magnetize at higher temperature than the larger domains. It also demonstrates how this effect could be transmitted by 'magnetic backwash' through the surrounding disordered phase in such a way that the larger ordered regions would receive a negative rather than a positive magnetization. This effect would be most efficient where the disordered intermediate regions are relatively narrow and lack space for wide magnetic domain walls.

Table 2 provides a list of the layers in Fig. 10 with their compositions, Q values, Curie Ts and theoretical magnetizations at 0 K. It also provides the cumulative magnetic moments based on 0 K as in Fig. 11(a), and cumulative moments based on a thermal model as in Fig. 11(b). Comments are provided linking the synthetic cooling curve Fig. 11(b) with the real cooling curves of Figs 2(a)–(c). In Fig. 11(b) the T_{PD} region begins with violet contact layer magnetization at ∼290 °C and continues through the temperature of 'magnetic backwash' to end at 140 °C, a very wide temperature range compared to Fig. 8(b). T_C is ∼232 °C, where positive magnetization begins to ramp up. Although only negative magnetizations are initiated below the lower limit of T_{PD} = ∼140 °C, positive magnetic intensity increase from cooling continues to dominate down to T_{MAX} at 117 °C. Below this, negative magnetization takes over and T_{ZM} is reached at 85 °C.

The chart in Fig. 11(a) and model in Fig. 11(b) show very abrupt features compared to Figs 8(a) and (b). The very sharp positive peak in Fig. 11(a) is related to the fact that 'backwash' was set to coincide at 140 °C with the Curie T of the six Ilm 64 layers of the A-ordered domain. The downward jog of the cooling curve of Fig. 11(b) between 150 and 135 °C relates directly to the backwash reversal of the right-hand wave. These irregularities would likely vanish in a model with a greater diversity of layers. We note again a difference at low T between the upward concavity of the synthetic curve and the downward concavity of the experimental curves in Figs 2(a)–(c). See Section 3.4 for speculations on possible origin of this.

4.3 Comments on composition estimates and the two-wave concept

Prévot *et al*. (2001), for a Pinatubo sample of composition X = 0.53, created a specific model of ordered domains embedded in a disordered matrix with Fe-enriched regions along the phase interface. In this respect, their model resembles the Fe-enriched waves in Fig. 10. They suggest the following magnetizations temperatures (T°C) and inferred compositions. Our own composition estimates for the same Ts are in italics. Disordered host 200 °C, X = 0.53 (*0.58*), disordered

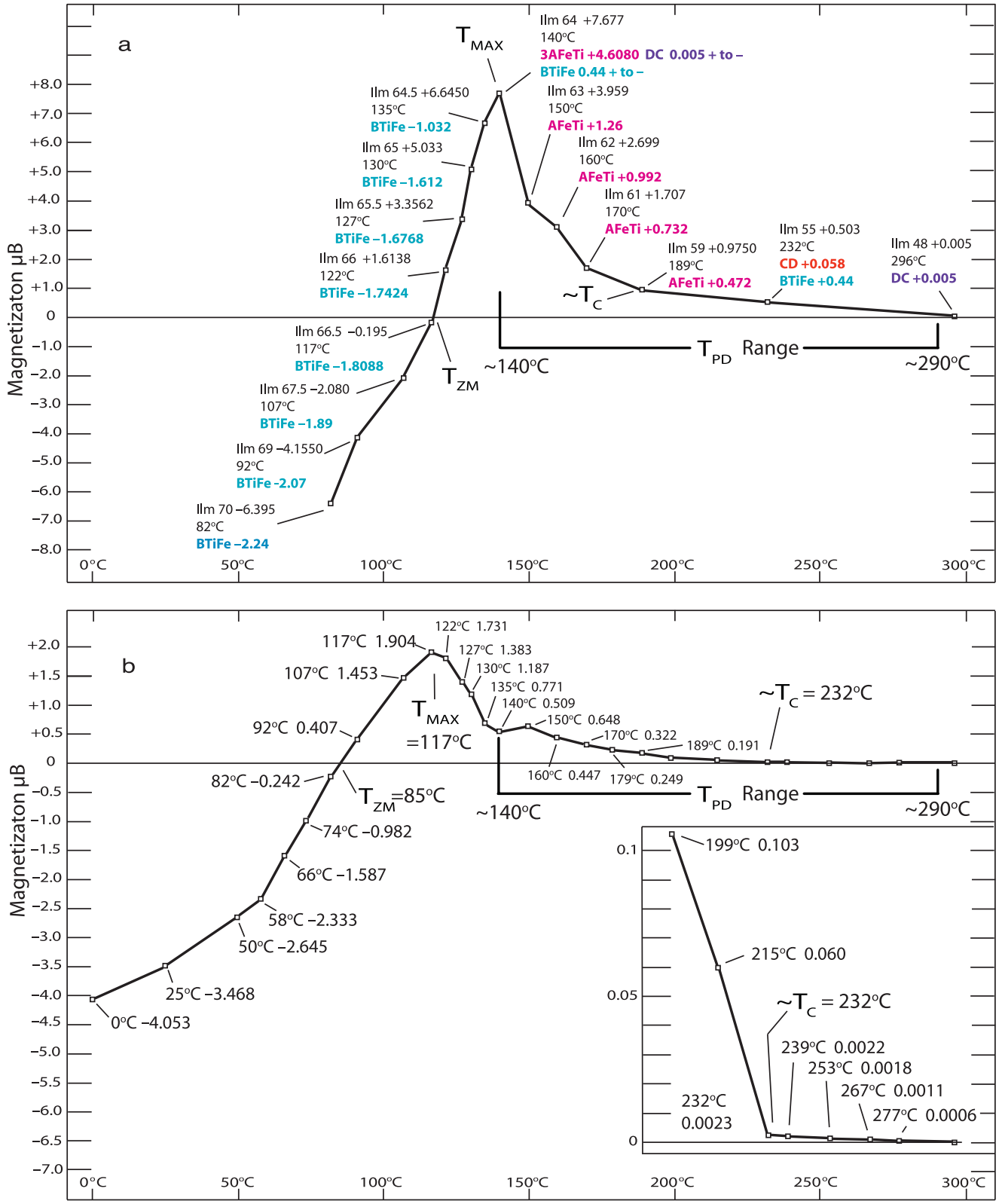

Figure 11. (a) Chart of progressive magnetic acquisition *T*s of layers in Fig. 10, magnetic moments of pairs of layers calculated at 0 K, and cumulative net magnetic moments as the magnetization *T*s are reached with falling *T*. Magnetic moments colour coded like layers in Fig. 10. A key feature at 140 °C is the reversal of positive magnetizations of the violet contact layer and the blue anti-ordered composition Ilm 55 to negative ('+ to –') resulting from 'magnetic backwash' shortly after complete magnetization of the A-ordered layers. (b) Synthetic cooling curve for Fig. 10). Magnetic intensity for each pair of layers is calculated in terms of a magnetic fraction based on the thermal difference at any *T* between the Curie *T* of the layer and 0 K. This fraction is 0 at the Curie *T* and 1.0 at 0 K. Intermediate values were determined using a thermal magnetic profile for hematite provided by Harrison.

Table 2. Layer compositions, *Q* values, magnetization *T*s and magnetic moments in Figs 10, 11(a) and (b).

Fig. 10 Layer Numbers	Fig. 10 Comp. (X)	Fig. 10 Q	Fig. 11A Mag. T^oC	Fig. 11A Mag. μB at 0 K	Fig. 11A Cum. Mag. μB at 0 K	Fig. 11B Cumulative Mag. μB at *T*	Fig. 11B Comment
41-42	*0.48*	*x*	*296*	*+0.005*			**+B Wave**
39-40	*0.48*	*0*	*296*	*0*			**Begin**
Total			**296**	**+0.005**	**+0.005**	**0.0**	**T_{PD}=290°C**
38-37	0.50	0	277	0	+0.005	+0.0006	
36-35	0.51	0	271	0	+0.005		
			267			+0.0011	
			253			+0.0018	
35-34	0.54	0	239	0	+0.005	+0.0022	
15-16	*0.55*	*x*	*232*	*+0.058*			**+A Wave**
17-20	*0.55*	*0*	*232*	*0*			
43-44	*0.55*	*–0.20*	*232*	*+0.44*			**Disorder**
Total			**232**	**+0.498**	**+0.503**	**+0.0023**	**T_C=232°C**
21-22	0.58	0	220	0	+0.503		
			215			+0.060	
			199			+0.103	
							Magnet-
14-13	0.59	+0.20	189	+0.472	+0.9750	+0.191	**ization**
23-32	0.60	0	179	0	+0.9750	+0.249	
12-11	0.61	+0.30	170	+0.732	+1.707	+0.322	
10-9	0.62	+0.40	160	+0.992	+2.699	+0.447	**A-Domain**
8-7	0.63	+0.50	150	+1.26	+3.959	+0.648	**Magneti-**
							zation
6-1	*0.64*	*+0.60*	*140*	*+4.6080*			
41-42	*0.48*	*x*	*140*	*–0.010*			
43-44	*0.55*	*–0.20*	*140*	*–0.88*			**Backwash**
Total				**+3.718**	**+7.677**	**+0.509**	**End T_{PD}=140°C**
45-46	0.645	–0.40	135	–1.032	+6.6450	+0.771	**B-Domain**
47-48	0.65	–0.62	130	–1.612	+5.033	+1.187	
49-50	0.655	–0.64	127	–1.6768	+3.3562	+1.383	**Magnet-**
51-52	0.66	–0.66	122	–1.7424	+1.6138	+1.731	**ization**
53-54	0.665	–0.68	117	–1.8088	–0.195	+1.904	**T_{MAX}=117°C**
55-56	0.675	–0.70	107	–1.89	–2.080	+1.453	
57-58	0.69	–0.75	92	–2.07	–4.1550	+0.407	
59-60	0.70	–0.80	82	–2.24	–6.395	–0.242	**T_{ZM}=85°C**
1-60			74			–0.982	
1-60			66			–1.587	
1-60			58			–2.333	
1-60			50			–2.645	
1-60			25			–3.468	
1-60			0			–4.053	

host rim <410 °C, X < 0.3 (*<0.36*), ordered domain rim 380 °C, X = 0.35 (*0.385*), core of ordered domain 270 °C, X = 0.54 (*0.517*). Except for their estimate for the disordered host composition, this suggests the same rim Fe-enrichment and ordered domain core depletion as portrayed in Fig. 10. To make sense, the disordered host must have an Fe-content substantially greater than the ordered core. Their magnetic model departs from ours in that: (1) They suggest that the Fe-enriched rims are oppositely magnetized compared to the cores. (2) They consider only one kind of ordered core, whereas we consider both A-ordering and B-anti-ordering as well as cores of different sizes and Fe-contents. (3) We think self-reversal is tied to simple antiferromagnetic interface interactions without significant involvement of spin-canted magnetization.

Lagroix *et al.* (2004) used magnetic data to try to distinguish compositions within their X = 0.70 quenched samples. They suggest a 107 °C magnetization temperature for the interiors of ordered domains in a disordered host, from which we infer a composition X = 0.675. Their estimates of 145 and 137 °C for partially disordered rims of such domains, imply more Fe-enriched compositions X = 0.637 and 0.645. Although their chemical model is limited, their interpretation favours antiferromagnetic coupling across phase interfaces.

5 DIVERGENT GROWTH OF ORDERED DOMAINS IN A DISORDERED MATRIX PROGRESSING TO COARSENING BY APB MOTION BETWEEN ORDERED AND ANTI-ORDERED DOMAINS

The chemical wave models of Figs 7 and 10 suggest a progression during annealing in which there is first growth of ordered domains against disordered domains, and then coarsening of some ordered domains and shrinking of others. Both processes can proceed in different places within the same sample, and, where the two chemical waves of Fig. 10 impinge, lead to the single wave shown in Fig. 7. In both figures it is the large B-anti-ordered region that is growing towards the left, first at the expense of the disordered region as in Fig. 10 and then at the expense of the A-ordered region as in Fig. 7. With the two waves converging into one, the Fe-enrichment of the single wave is larger than in the double wave. An interesting further consequence would be in the situation where two growing B-anti-ordered regions converge on a disordered region and eventually extinguish it by merger. One might expect an especially strong Fe-enrichment at such at extinction point, where the Fe either has to diffuse away into the adjacent ordered phase, or remain at a sort of Fe-rich corner.

The concepts discussed in the previous paragraph are used in Figs 12 and 13 for the construction of colour contour maps of Fe content of different types of composition waves. Attention is called to the fact that the chemical composition range implied by the magnetic models of Figs 7 and 10 is fairly similar to the range we recorded with TEM, that is, Ilm 50–70 (Fabian *et al*. 2011). Because the T_{PD} range is determined mainly by the Fe-rich parts of the waves including disordered layers near contact layers, it is not surprising to find that T_{PD} of most samples with bulk composition Ilm 60–65 imply wave compositions Ilm 55–45. Our new magnetic results favour chemical phase separations even greater than we envisioned. The well ordered and anti-ordered regions observed by TEM are less than 7 nm across, which complicates phase analysis by standard X-ray diffraction (XRD) methods. The samples appear to be dominated by disordered regions of relatively homogenous composition (Fig. 10), which would give intense sharp peaks in XRD. However diffraction from the minority part of the samples showing the ordered domains, already broadened due to the small size, will further be broadened and weakened in intensity by the compositional range. As a result the very weak broad diffraction from the ordered regions is smeared out in the background and so the chemical phase separation is not possible to detect with normal XRD (Fabian *et al*. 2011).

Fig. 12 shows a small part of a chemical landscape produced by arrested chemical evolution. Fig. 12(a) shows the temporal positions of chemical wave crests at the boundaries of growing ordered domains. The domain to the upper left is a small and slowly growing A-ordered domain like the small domain to the left in Fig. 10. Relatively slow growth is indicated by relatively close spacing of the colour-coded wave crest at times 1–11, probably reflecting late nucleation of order within a disordered area. The domain to the upper right is a large and more rapidly growing B-anti-ordered domain like the large domain to the right of Fig. 10. More rapid growth is indicated by relatively wider spacing of the colour-coded wave crests at times 4–11, probably reflecting early nucleation of order within a disordered area far to the northeast outside the map area. The wave crests are converging towards each other with time, close to convergence at time 7 and converged at time 8. With convergence, the double-wave profile of Fig. 10, is represented by wave positions

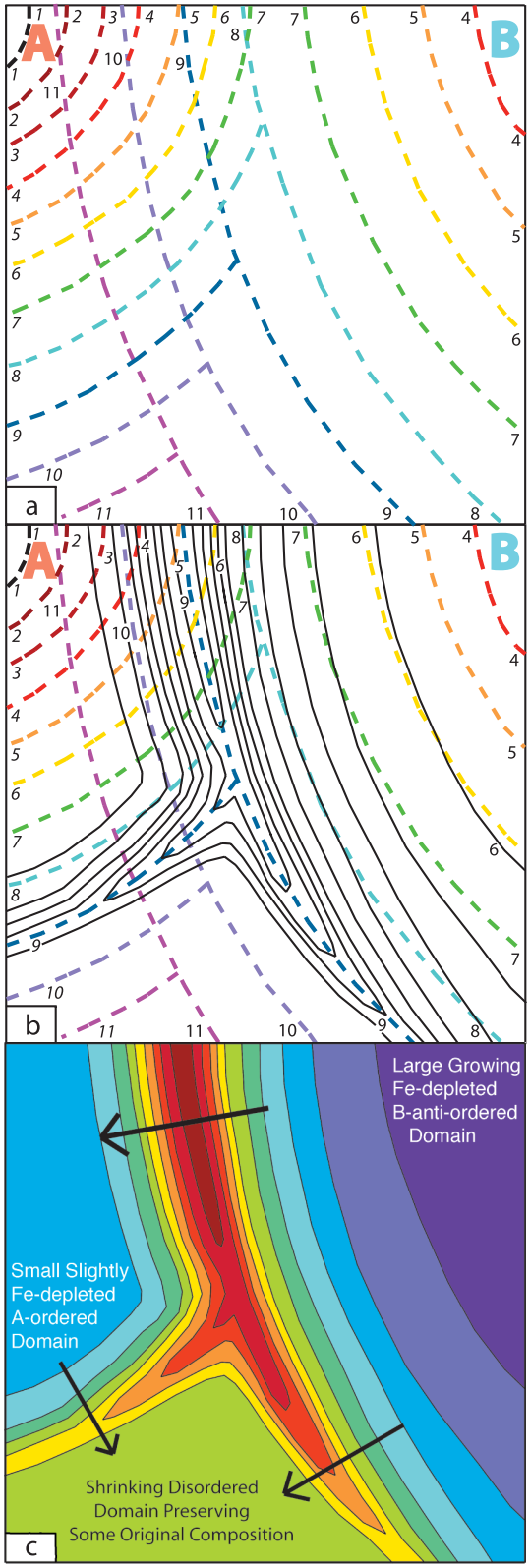

Figure 12. (a) Areal map showing progressive positions of phase boundaries at times 1–11 during quench and annealing (see text). (b) The same map as (a) with chemical evolution arrested with the phase boundaries at time 8, and schematic contours of Fe content added. (c) The same map as (b). Time lines removed. Fe-contour intervals coloured (darkest red highest, violet lowest). Each of the three domains described and the directions of movement of the composition waves indicated.

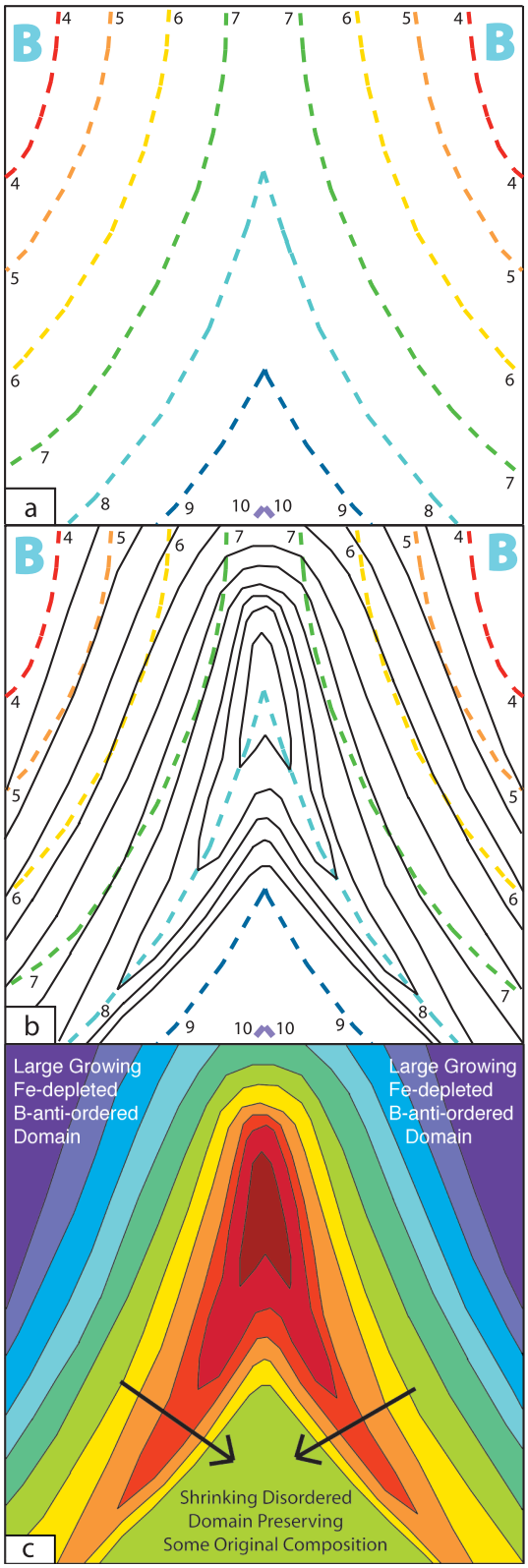

Figure 13. (a) Areal map showing progressive positions of phase boundaries at times 4–10 during quench and annealing (times 1–3 outside the map). (b) The same map as (a), with chemical evolution arrested at time 8 and schematic contours of Fe content added. (c) The same map as (b). Time lines removed. Fe-contour intervals coloured (darkest red highest, violet lowest). Each of three domains described and the directions of movement of the composition waves indicated.

in the lower part of Fig. 12(a). In the upper part of Fig. 12(a) this is replaced by a single-wave profile as in Fig. 7. Above the convergence, the large B-anti-ordered domain continues to grow, whereas the small A-ordered domain begins to shrink. Convergence can continue to where the growth-wave crest of the B-anti-ordered domain progressively intersects and extinguishes the growth-wave crest of the A-ordered domain.

The growth-wave pattern of Fig. 12(a) is used to construct a qualitative Fe-content contour map of the system in Fig. 12(b), when chemical evolution is arrested at time 9. Fig. 12(c) shows the resulting Fe-content contours (highest in dark red, lowest in violet) for this stage of evolution, with the progressive growth-wave crests removed. Each of the three relevant domains is described and the directions of arrested chemical wave movement are indicated. We see that Fe-enrichment is least along the growth waves in the lower left and bottom of the figure, much greater where the growth waves have converged, and still greater where the B-anti-ordered domain is growing and the A-ordered domain is shrinking.

Two key observations derive from Fig. 12(c). (1) In samples with intermediate stages of textural evolution during quench and annealing, all three types of waves should be expected. (2) Within these waves there will be a rather rich variety of compositions with different Fe contents and therefore different magnetization temperatures. All these will inevitably be integrated into the total picture of T_{PD} range and progressive acquisition of thermoremanent magnetization.

An additional aspect of chemical landscape evolution is illustrated in Fig. 13. Fig. 13(a) shows the temporal positions of composition waves on the borders of two growing large B-anti-ordered domains, coincidentally of the same size and growth rate. The waves have not impinged by time 7, but have impinged by time 8. Here impingement implies complete chemical merger of two chemical domains with eventual extinction of the related chemical waves between them. Fig. 13(b) shows qualitative Fe-content contours on the two converging chemical waves arrested at time 8.

Fig. 13(c) shows the resulting Fe-content contours for this stage of evolution with the progressive growth-wave crests removed. As in Fig. 12(c), Fe-enrichment is weakest in the region of least wave convergence at the bottom of the figure and reaches maximum value in the region of wave convergence in the upper middle. Exactly what happens in the region of complete merger of the two B domains is not certain. Possibly the Fe-enrichment in the junction region becomes progressively more extreme, which would, provide progressively more Fe-rich compositions in terms of local higher magnetization *T*s. More probably, with conditions above the equilibrium solvus, these gradients should disappear as the gradients in Q disappear in the two B domains.

The conceptual Fe-content landscapes provided in Figs 12(c) and 13(c) are only small parts of a larger landscape in which both types of junctions will be present inevitably. Such broader landscapes could be constructed based on the ideas presented here, balanced in terms of bulk chemical composition and total magnetic evolution. More fruitful, and an obvious next step, will be proper simulations of the ordering/coarsening process.

6 CONCEPTUAL MODEL AND EXPERIMENTAL CURVES

In light of the conceptual models presented above, it is interesting to go back to the experimental results in Figs 1 and 2. The 'T_{PD}' ranges from Figs 1(a) and (b) are 285–250 °C and 255–150 °C, respectively,

corresponding to composition ranges Ilm 49–53 (bulk composition Ilm 60) and Ilm 52.5–63 (bulk composition Ilm 65). The broad range of T_{PD}'s agrees with the idea that, when the pre-destination is locked in along the phase boundaries, the compositions on the boundaries are quite variable. This is consistent with a spatially complex pattern of ordered domain growth and coarsening relating to 'waves' with highly varied Fe-enrichment.

Several observations can be made when comparing these results with the corresponding magnetic cooling curves in Figs 2(a) and (b). In both examples, the upper end of the T_{PD} range comes at a temperature well above the T_C related to a significant fraction of ferrimagnetic material, where the magnetization is weak. This can perhaps be related to the fact that the modelled contact layer ferrimagnetic moment is weak and is closely tied with magnetization of adjacent disordered layers. In the example of Fig. 2(a) the lower end of the T_{PD} range comes at a point where the initial positive magnetization is still ramping up. In Fig. 2(b), by contrast, the lower end of the T_{PD} range comes almost exactly at T_{MAX}. A similar T_{PD} range is shown in Fig. 11(b) for the chemical-wave model in Fig. 10, though it does not extend down to T_{MAX}. This would correspond to the postulated condition where the 'magnetic backwash' through a large disordered domain reaches the right-hand chemical wave, causing magnetic reversal of the contact layer. The TEM image of B-20 in Fig. 6(B) suggests that this sample could contain a significant fraction of disordered phase, consistent with the double-wave model. This cannot be verified because much of the dark area of this image may represent poor order rather than disorder. However, the same can be said for B-06, with the small T_{PD} range. An alternative interpretation for the cooling curve of the Ilm 65 composition of sample B-20 in Fig. 2(b) is that chemical evolution has progressed farther, to the stage where small Fe-enriched domains have shrunk from movement of APB's, leaving a greater proportion of Fe-depleted domains with self-reversed magnetization, but also leaving APB waves with highly varied compositions. Our growing collection of cooling and T_{PD} curves for samples Ilm 60, 65 and 70 with different quench temperatures and annealing Ts and times, suggests arrested composition landscapes with considerable interface complexity.

7 CONCLUSIONS

Magnetic experiments on a series of synthetic ferri-ilmenite samples in the bulk composition range Ilm 60–70 quenched and annealed at high temperatures (T), well above any magnetization T, throw new light on metastable chemical phenomena leading to fine-structure in the acquisition of thermoremanent magnetization. Growth of Fe-Ti ordered domains in a disordered host, or growth and shrinking of adjacent Fe-Ti ordered domains against each other in the process of coarsening, lead to Fe-enrichment in some domains relative to others, influencing magnetization T. Additional Fe-enrichment along domain boundaries during these processes produces Fe-enriched waves on the boundaries, where ferrimagnetic material near the wave crests, magnetizes at a higher T than the bulk of the sample. Because the boundaries are APBs with opposite Fe-Ti ordering, opposite sides must acquire opposite magnetic moments during cooling, at a T above that where bulk normal magnetization begins. This is the 'magnetic pre-destination T' or 'T_{PD}', because it sets the stage for normal and self-reversed magnetization on opposite sides of the phase domain boundary. The Fe-enrichment waves are not uniform in a sample; neither are the compositions along the domain walls. Generally 'T_{PD}' is not a single T, but a T range, and reflects only a small volume of the sample. With further cooling in a positive field, slightly less Fe-enriched, but more voluminous ferrimagnetic regions start to magnetize, leading to a positive magnetic peak, 'T_{MAX}'. Already here, even less Fe-enriched but still more voluminous ferrimagnetic material, influenced by the domain wall, begins to acquire self-reversed magnetization. This dominates in cooling below 'T_{MAX}', eventually leading to dominantly self-reversed magnetization below 'T_{ZM}'. A conventional Curie T obviously cannot be measured meaningfully from a cooling curve in this material of varied composition; a graphically convenient point (T_C) only gives a value for a significant fraction of material of composition where the normal thermoremanent magnetization is acquired. The Fe-enriched chemical waves on phase boundaries described here, that set the stage for acquisition of self-reversed thermoremanent magnetization in further cooling, are tantalizing close in position, though not in concept, to the 'x-phase' on phase boundaries that Nord and Lawson thought to be the key to self-reversal.

ACKNOWLEDGEMENTS

This paper is dedicated to our long-term friend and collaborator, Gordon Nord. Twenty-five years ago, he, along with C. A. Lawson, provided the critical TEM studies linked to magnetic measurements that began to unlock the key essentials of self-reversed thermoremanent magnetization. This and related research was supported by grant 189721 from the Research Council of Norway (Nanomat Program) in the EU Matera Program, and visiting fellowships to the Institute of Rock Magnetism, which is supported by an NSF Instruments and Facilities Grant. Collaboration and creative suggestions were provided by our research partner, Prof Helmer Fjellvåg, University of Oslo. Katja Svendby at NGU was of great assistance in the magnetic experiments. The manuscript was improved by suggestions from two anonymous reviewers. To each of these persons and institutions we extend our grateful acknowledgement.

REFERENCES

Fabian, K., Miyajima, N., Robinson, P., McEnroe, S.A., Boffa Ballaran, T. & Burton, B.P., 2011. Chemical and magnetic properties of rapidly cooled metastable ferri-ilmenite solid solutions: implications for magnetic self-reversal and exchange bias, I. Fe-Ti order transition in quenched synthetic ilmenite 61, *Geophys. J. Int.,* **186,** 997–1014.

Harrison, R.J., 2006. Microstructure and magnetism in the ilmenite-hematite solid solution: a Monte Carlo simulation study, *Am. Miner.,* **91,** 1006–1023.

Harrison, R.J., Kasama, T., White, T.A., Simpson, E.T. & Dunin-Borkowski, R.E., 2005. Origin of self-reversed thermoremanent magnetization, *Phys. Rev. Lett.,* **95,** 268501.

Hoffman, K.A., 1975a. Cation diffusion processes and self-reversal of thermo-remanent magnetization in the ilmenite-haematite solid solution series, *Geophys J. R. astr. Soc.,* **41,** 65–80.

Hoffman, K.A., 1975b. On the kinetics of cation ordering in hemoilmenites and a re-examination of the self-reversal process, *EOS, Trans. Am. geophys. Un.,* **56,** 975.

Hoffman, K.A., 1992. Self-reversal of the thermo-remanent magnetization in the ilmenite-hematite system: order-disorder, and spin alignment, *J. geophys. Res.,* **97,** 10 883–10 895.

Ishikawa, Y. & Akimoto, S., 1957. Magnetic properties of the $FeTiO_3$-Fe_2O_3 solid solution series, *J. Phys. Soc. Jpn.,* **12,** 1083–1098.

Ishikawa, Y. & Syono, Y., 1963. Order-disorder transformation and reverse thermo-remanent magnetism in the $FeTiO_3$-Fe_2O_3 series, *J. Phys. Chem. Solids,* **24,** 517–528.

Lagroix, F., Banerjee, S.K. & Moskowitz, B.M., 2004. Revisiting the mechanism of reversed thermoremanent magnetization (rTRM) based on

observations from synthetic ferrian ilmenite (y = 0.7), *J. geophys. Res*., **109**(B12), doi:10.1029/2004JB003076.

Meiklejohn, W.H. & Carter, R.E., 1959. Exchange anisotropy in rock magnetism, *J. appl. Phys.,* **30,** 2020.

Nagata, T., Uyeda, S. & Akimoto, S., 1952. Self-reversal of thermoremanent magnetism in igneous rocks, *J. Geomag. Electr.,* **4,** 22–38.

Nord, G.L. Jr. & Lawson, C.A., 1989. Order-disorder transition-induced twin domains and magnetic properties in ilmenite-hematite, *Am. Mineral.,* **74,** 160–176.

Nord, G.L. Jr. & Lawson, C.A., 1992. Magnetic properties of ilmenite 70-hematite 30: effect of transformation-induced twin boundaries, *J. geophys. Res.,* **97,** 10 897–10 910.

Ozima, M., Oshima, O. & Funaki, M., 2003. Magnetic properties of pyroclastic rocks from the later stage of the eruptive activity of Haruna Volcano in relation to the self-reversal of thermo-remanent magnetization, *Earth Planets Space,* **55,** 183–188.

Prévot, M., Hoffman, K.A., Goguitchaichvili, A., Doukhan, J.-C., Shcherbakov, V. & Bina, M., 2001. The mechanism of self-reversal of thermoremanence in natural hemoilmenite crystals: new experimental data and model, *Phys. Earth planet. Int.,* **126,** 75–92.

Robinson, P., Harrison, R.J. & McEnroe, S.A., 2006. Fe2+/Fe3+ charge ordering in contact layers of lamellar magnetism: bond valence arguments, *Am. Mineral.,* **91,** 67–72.

Robinson, P., Fabian, K. & McEnroe, S.A., 2010. The geometry of ionic arrangements and magnetic interactions in ordered ferri-ilmenite solid solutions and its effect on low-temperature magnetic behavior, *Geochem., Geophys., Geosyst.,* **11,** Q05Z17, doi:10.1029/2009GC002858.

Robinson, P., Harrison, R.J., Miyajima, N., Suzanne, A., McEnroe, S.A. & Fabian, K., 2012a. Chemical and magnetic properties of rapidly cooled metastable ferri-ilmenite solid solutions: implications for magnetic self-reversal and exchange bias, II. Chemical changes during quench and annealing, *Geophys. J. Int.,* **188,** doi:10.1111/j.1365-246X.2011.05277.x.

Robinson, P., Fabian, K., Harrison, R.J. & McEnroe, S.A., 2012b. Chemical and magnetic properties of rapidly cooled metastable ferri-ilmenite solid solutions: implications for magnetic self-reversal and exchange bias, III. Magnetic interactions in samples produced by Fe-Ti ordering, *Geophys. J. Int.,* **188,** 1025–1047.

Uyeda, S., 1958. Thermo-remanent magnetization as a medium of paleomagnetism, with special reference to reverse thermo-remanent magnetism, *Jpn. J. Geophys.,* **2,** 1–123.